Dynamic In-Hand Sliding Manipulation

Jian Shi, J. Zachary Woodruff, *Student Member, IEEE*, Paul B. Umbanhowar, and Kevin M. Lynch, *Fellow, IEEE*

***Abstract*—This paper presents a framework for planning the motion of an n-fingered robot hand to create an inertial load on a grasped object to achieve a desired in-grasp sliding motion. The model of the sliding dynamics is based on a soft-finger limit surface contact model at each fingertip. A motion planner is derived to automatically solve for the finger motions for a given initial and desired configuration of the object relative to the fingers. Iterative planning and execution are shown to reduce the errors that occur due to the modeling and trajectory tracking errors. The framework is applied to the problem of regrasping a laminar object held in a pinch grasp. We propose a limited surface model of the contact pressure distribution at each finger to predict the sliding directions. Experimental validations are shown, including iterative error reduction and repeatability of the experiment.**

***Index Terms*—Dexterous manipulation, dynamics, grasping, in-hand manipulation, manipulation planning.**

I. Introduction

A. Background

MOST human, animal, and even robot manipulation tasks involve controlling motion of the object relative to the manipulator, particularly in nonprehensile (graspless) manipulation modes such as pushing, rolling, pivoting, tipping, tapping, and kicking. Even in pick-carry-place manipulation, in which the carry portion of the task keeps the object stationary relative to the hand, the pick and place phases typically involve the object sliding or rolling on the fingers as the hand achieves a firm grasp or releases the object. Other examples of controlled relative motion in grasping manipulation include finger gaiting, in which the fingers quasi-statically walk over the object to achieve a regrasp, all the while maintaining a stable grasp, rolling the object on the fingertips, and letting the object slide relative to the fingertips. Together we refer to these types of relative motion as *in-hand manipulation*.

We are studying in-hand manipulation by controlled sliding for three purposes:

Manuscript received August 5, 2016; revised January 18, 2017; accepted March 12, 2017. Date of publication April 27, 2017; date of current version August 7, 2017. This paper was recommended for publication by Associate Editor J. Piater and Editor A. Billard upon evaluation of the reviewers' comments. This work was supported by the National Science Foundation under Grant IIS-0964665, Grant IIS-1527921, and Grant DGE-1324585. *(Corresponding author: Jian Shi.)*

J. Shi, J. Z. Woodruff, and P. B. Umbanhowar are with the Neuroscience and Robotics Laboratory, Northwestern University, Evanston, IL 60208 USA (e-mail: JianShi@u.northwestern.edu; jzwoodruff@u.northwestern.edu; umbanhowar@northwestern.edu).

K. M. Lynch is with the Neuroscience and Robotics Laboratory, Northwestern University, Evanston, IL 60208 USA, and is also with the Northwestern Institute on Complex Systems, Evanston, IL 60201 USA (e-mail: kmlynch@northwestern.edu).

Color versions of one or more of the figures in this paper are available online at http://ieeexplore.ieee.org.

Digital Object Identifier 10.1109/TRO.2017.2693391

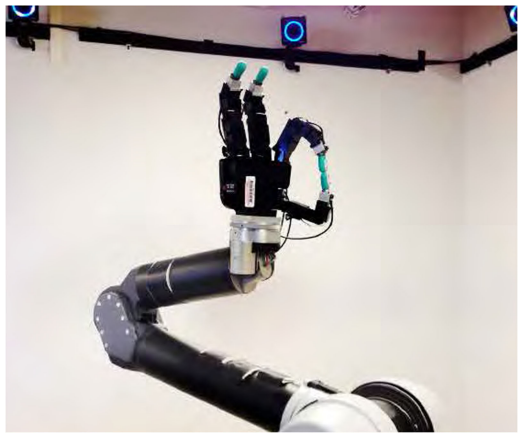

Fig. 1. ERIN instrumented manipulation environment, showing the WAM arm, the Allegro hand, four BioTac tactile sensing fingertips, and part of the 10-camera *OptiTrack* motion capture system. In this work, we replace the Allegro hand and tactile sensors with a lightweight parallel gripper as discussed in Section VIII and shown in Fig. 9.

1) Error-corrective sliding in an assembly task: The problem is to choose a grasp configuration satisfying force-closure constraints as well as providing error-corrective sliding motion in response to likely disturbance forces during the place operation. For example, uncertainty in a peg-in-hole assembly task results in contact forces that should be mapped to error-corrective motion, using the remote center of compliance device [1] or using active accommodation control [2]. Alternatively, it is possible to use sliding at the fingertips as the source of compliance. By the choice of finger locations and normal forces, we can control the shape of the grasp *limit surface* (see Sections II and V), which governs the mapping from contact forces to sliding directions, much like an accommodation control law maps contact forces to corrective velocities.

2) Regrasping using external contacts: The goal of the previous task is to achieve a desired object configuration relative to external fixtures. In this task, the goal is to achieve a desired object configuration relative to the hand. Contact with the environment is used to generate forces that cause the object to slide relative to the fingers to a desired new grasping configuration. A manually designed example of this task can be found in [3].

3) Regrasping using dynamic loads: In the previous task, the forces causing the regrasp come from contact. In this task, the hand uses object inertia to cause it to slide to the desired new grasp by accelerating the hand beyond the point the finger friction forces can resist relative motion.

This paper focuses on the last problem: accelerating the hand to achieve a desired regrasp. Our testbed is the ERIN robot manipulation system as shown in Fig. 1. Assuming the fingers

are compliantly mounted, and the initial grasp configuration is chosen, current research problems include:

1) given the state of the hand and object, the contact normal forces, and the acceleration of the hand, find the relative acceleration of the object (forward dynamics);
2) given the state of the hand and object and the desired relative acceleration of the object, find appropriate hand accelerations and contact normal forces (inverse dynamics);
3) plan the hand motion (and possibly contact normal forces) to achieve a desired regrasp;
4) repeatedly plan and execute hand motions to iteratively reduce grasp error;
5) use real-time feedback control of hand motion and finger normal forces during sliding motion to achieve the desired regrasp; and
6) estimate friction properties from observed hand and object motions, given the contact normal forces.

In this study, we use a simple, spring-actuated passive hand in place of the Allegro hand and tactile sensors, and we study items (1)–(4) above. In particular, we focus on the case of planar motion, in which the laminar object moves with three degrees of freedom (two translational and one rotational) and the fingers contact the object on opposite sides that are parallel to the plane of motion. This paper extends our preliminary work reported in [4].

B. Paper Outline

Section II reviews previous work on which this paper builds. In Section III, we solve problems (1)–(4) for a simple 1-DOF example, as a template for the more general case. In Section IV, we generalize the problem statement to an n-fingered grasp moving in a plane. In Section V, we discuss the limit surface model for friction and derive expressions for the frictional wrench given the sliding velocity of an object in an n-fingered grasp consisting of patch contacts. In Section VI, we derive the sliding dynamics within the motion plane and outline a method to calculate the acceleration of the object relative to each finger given the accelerations of the fingers. In Section VII, we solve the finger motion planning problem for a given n-fingered grasp to achieve a desired regrasp.

The material in Sections IV–VII solves the planar regrasp problem for general n-fingered grasps of an object with parallel faces. The details of the finger normal forces and grasp limit surface depend on the particular grasp configuration, however. In Section VIII, we derive the details of the grasp limit surface for a particular type of grasp, a two-fingered pinch grasp. In Section IX, we implement the motion planning algorithm for in-hand manipulation with a two-fingered pinch grasp, and we show experimentally that iterative planning and execution can further reduce error in the final grasp configuration.

II. Related Work

A. In-Hand Manipulation

There has been extensive work on kinematic in-hand manipulation where an object is moved relative to a finger without breaking contact or sliding on the surface. This is sometimes referred to as precision manipulation. Li *et al.* [5] and Yoshikawa and Nagai [6] used rigid, rolling finger contacts to calculate grasp stability and manipulability, and to develop controllers for tracking a position trajectory while maintaining a desired grasp force. More recent related work by Rojas and Dollar [7] estimated the precision manipulation capabilities of arbitrary manipulator/object configurations for use in autonomous manipulation planning.

In-hand sliding manipulation can also be used to quickly reposition an object in the hand. Traditional dexterous regrasp methods such as finger gaiting or "pick" and "place" may be slow or impossible given the number of fingers or the surrounding environment. Brock [8] addressed the problem of controlled sliding by first generating a constraint state map that outlines constraints on a grasped object due to the contact types and forces. By varying the contact forces he achieved controlled sliding in desired directions for a grasped cylinder. Cole *et al.* [9] explored a dynamic coordinated control scheme to reposition objects with controlled slip. Trinkle and Hunter [10] extended the dexterous manipulation planning problem to consider rolling and slipping contact modes. The hybrid planning problem was further developed by Yashima *et al.* [11]. The space of reachable object states can be further expanded by breaking contact with a single finger, moving it, and regrasping the object while the remaining fingers maintain the object in force closure. This in-hand regrasp technique is called finger gaiting [12]–[13].

Dynamic forces can also be used for in-hand manipulation. Furukawa *et al.* [14] demonstrated regrasping by tossing a foam cylinder up and catching it. Chavan-Dafle *et al.* [3] tested hand-coded regrasps that take advantage of external forces such as gravity, dynamic forces, and contact with the environment to regrasp objects using a simple manipulator. A more recent work by Chavan-Dafle *et al.* [15] explored in-hand manipulation of an object by external contacts with the environment. With designed finger actions, motions of the object were simulated and validated experimentally with different shapes of contacts. Viña *et al.* [16]–[17] showed that by using adaptive control with vision and tactile feedback, monodirectional pivoting of an object pinched by a pair of fingers can be achieved by changing the gripping forces. Kumar *et al.* [18] programmed a pneumatically actuated hand to learn in-hand manipulation skills using model-based reinforcement learning. Sintov and Shapiro [19] developed an algorithm to swing up a rod by generating gripper motions, in which the contact point was modeled as a pivot joint that can apply frictional torques. The method was validated in simulation. Hou *et al.* [20] studied dynamic planar pivoting of a pinched object driven by the hand swing motion and contact normal force control.

Arisumi *et al.* [21] explored casting manipulation where a manipulator is thrown and its "free flight" trajectory is controlled in midair using tension forces on a tether. Similarly, dynamic in-hand sliding motions allow the manipulator to impart forces on the object during motion. This allows for feedback control and the ability to quickly regrasp the object at any point throughout the trajectory.

B. Friction Modeling

Goyal *et al.* [22]–[24] describe the concept of a limit surface as a 2-D surface in a 3-D force–moment space. The limit surface defines the maximum set of external wrenches that can be resisted by the frictional forces due to the contact. Xydas and Kao [25] derived models of soft-finger contacts and the resulting limit surfaces. Recent work by Zhou *et al.* [26] proposed a fourth-order polynomial limit surface model for planar sliding and identified model parameters using simulation and experimental data.

III. 1-DOF Example

In this section, we address research topics (1)–(4) from the introduction for a 1-DOF example with no gravity. This example serves as a template for the more general problem beginning in Section IV.

Consider an object that accelerates in the positive or negative direction due to frictional contact with a single finger. Based on a Coulomb friction coefficient μ and a normal force f_N, the finger can provide a tangential force to the object of up to μf_N before sliding. We assume the object has unit mass, so the maximum object acceleration is $a_o = \mu f_N$. We also assume the finger is capable of a maximum acceleration $a_f > a_o$. Additionally, we define a finger acceleration a greater than 0 but less than a_o. The relationship between the accelerations can be written as $a_f > a_o > a > 0$.

Let $q_f(0) = q_o(0)$ be the initial position of the finger and the object w.r.t. the world frame $\mathcal{W}$ respectively, and let $d(t) = q_o(t) - q_f(t)$ be the object position relative to the finger position at time t. The problem is to choose a finger acceleration profile $\ddot{q}_f : [0, T] \to \mathbb{R}$ that causes the object to slide relative to the finger by d_{goal} at time T, i.e., $d(T) = q_o(T) - q_f(T) = d_{\text{goal}}$ as shown in Fig. 2. Without loss of generality, assume $d_{\text{goal}} > 0$. Similar reasoning applies for the case $d_{\text{goal}} < 0$.

A. Forward Dynamics

The forward dynamics problem is to determine the relative sliding acceleration $\ddot{d}$ given a finger acceleration $\ddot{q}_f$. If $\dot{d} \neq 0$, then $\ddot{d} = \text{sgn}(\dot{d})a_o - \ddot{q}_f$. If $\dot{d} = 0$ and $|\ddot{q}_f| \leq a_0$, no sliding occurs ($\ddot{d} = 0$). If $\dot{d} = 0$ and $|\ddot{q}_f| > a_0$, then $\ddot{d} = \text{sgn}(\ddot{q}_f)a_0 - \ddot{q}_f$.

B. Inverse Dynamics

The inverse problem is to determine the finger acceleration $\ddot{q}_f$ that achieves a desired relative sliding acceleration $\ddot{d}$. If $\dot{d} \neq 0$, then $\ddot{q}_f = \text{sgn}(\dot{d})a_o - \ddot{d}$. If $\dot{d} = \ddot{d} = 0$, no slip occurs so any $|\ddot{q}_f| \leq a_o$ is valid. If $\dot{d} = 0$ and $|\ddot{d}| > 0$ (you are trying to initiate slip), then $\ddot{q}_f = \text{sgn}(\ddot{d})a_0 - \ddot{d}$.

C. Motion Planning

We assume the finger and object are initially at rest and $q_f(0) = q_o(0) = 0$, and require that the finger's net displacement and velocity after the motion are zero. To achieve the sliding regrasp while satisfying these constraints, we first accelerate the finger with $\ddot{q}_f = a$ for time T_1. We then apply the maximum negative acceleration $\ddot{q}_f = -a_f$ for time T_2. Next we apply $\ddot{q}_f = a$ for time $T_3 + T_4 = T_{34}$. To achieve zero final displacement and velocity for the finger, we choose $T_1 = T_{34}$ and $\dot{q}_f(T_1) = -\dot{q}_f(T_1 + T_2)$.

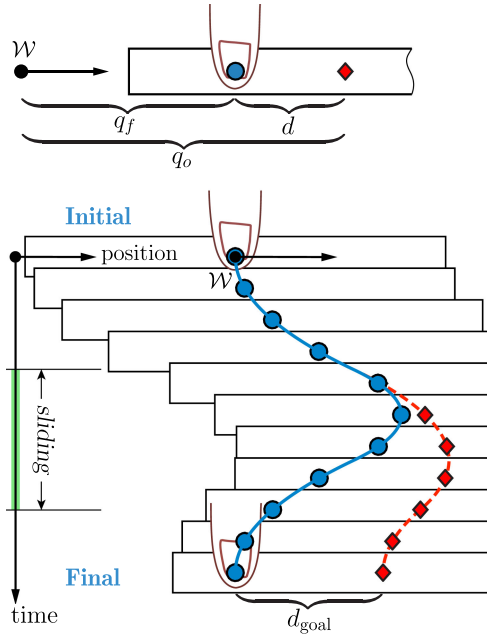

Fig. 2. (Top) Configuration of the 1-DOF system. The red diamond shows the center of mass (CM) of the object and the blue dot shows the contact point of the finger. (Bottom) An example of in-hand sliding of the 1-DOF system with initial condition $q_f(0) = q_o(0) = 0$. The finger initially accelerates to the right, and then accelerates to the left causing the finger to slide on the object and achieve a desired position relative to the object CM d_{goal}. The corresponding acceleration, velocity, and position profiles are shown in Fig. 3.

The motion plan consists of three phases: an initial sticking phase of duration T_1, a sliding phase of duration $T_2 + T_3$, and a final sticking phase of duration T_4. During phase 1 ($0 \leq t < T_1$), $\dot{d}$ is zero and $|\ddot{q}_f| \leq a_o$ so no relative motion occurs. During the first part of phase 2 ($T_1 \leq t < T_1 + T_2$), the negative acceleration is sufficiently high that sliding occurs ($\ddot{q}_f < -a_o$). During the second part of phase 2 ($T_1 + T_2 \leq t < T_1 + T_2 + T_3$), the acceleration magnitude is decreased ($|\ddot{q}_f| \leq a_o$), but $\dot{d} \neq 0$ so sliding still occurs until $\dot{d} \to 0$. During phase 3 ($T_1 + T_2 + T_3 \leq t < T_1 + T_2 + T_3 + T_4$), the object is sticking and $\dot{d} = 0$. Fig. 2 shows an example of in-hand sliding of the 1-DOF system. The full series of accelerations, resulting velocities, and positions are shown in Fig. 3.

The total relative sliding distance d_{goal} is the integral between the finger and object velocity curves in the sliding phase. With given values of a_f, a_o, a, and d_{goal}, we solve the following constraints to find the durations T_1, T_2, T_3, and T_4:

$$2aT_1 = a_f T_2 \tag{1}$$

$$a_o(T_2 + T_3) = a(2T_1 - T_3) \tag{2}$$

$$d_{\text{goal}} = 0.5(a_f - a_o)(T_2^2 + T_2 T_3) \tag{3}$$

$$T_4 = T_1 - T_3. \tag{4}$$

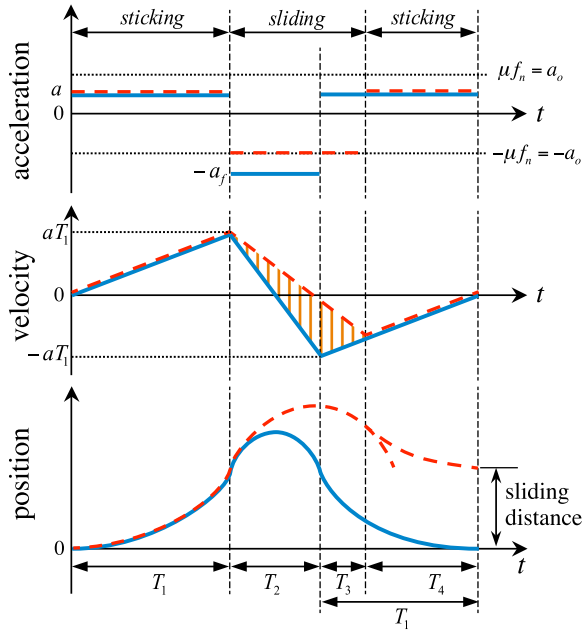

Fig. 3. Plot of the system motion profile of the 1-DOF problem. The solid blue curves represent the motion of the finger and the dashed red curves represent the motion of the object. The object has unit mass. In the velocity profile, the orange shaded area is the relative sliding distance.

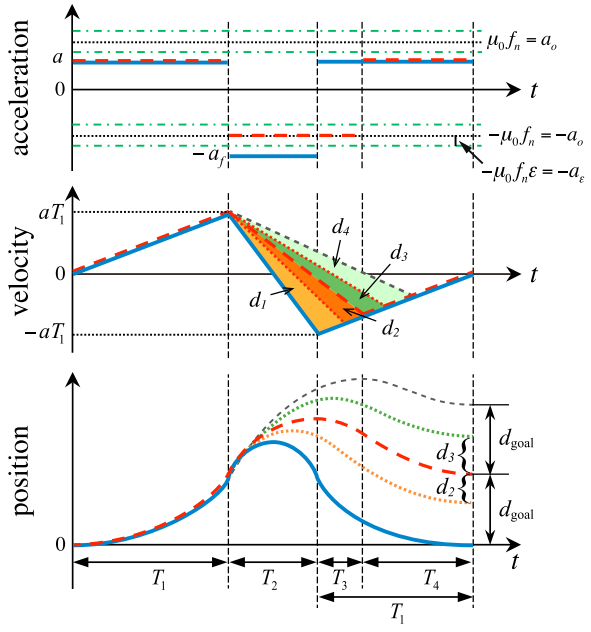

Fig. 4. Friction uncertainty affects the sliding distance. We denote d_1, d_2, d_3, d_4 as the areas of different triangles and $d_1 + d_2 = d_3 + d_4 = d_{\text{goal}}$. The areas d_2 and d_3 show the uncertainty in the sliding distance. Area d_2 represents the error when the friction coefficient is underestimated, and d_3 represents the overestimated case.

Equation (1) enforces that the finger velocity at time $T_1 + T_2$ is the opposite of the finger velocity at time T_1. Equation (2) requires the object to stop slipping relative to the finger at time $T_1 + T_2 + T_3$. Equation (3) enforces the desired slipping distance of the object. Together, (1), (2), and (4) ensure the total finger displacement is zero after the regrasp motion. The chosen constraints ensure that T_1, T_2, T_3, and T_4 can be solved for analytically, which simplifies the 1-DOF problem. We can solve (1)–(3) for T_1, T_2, T_3 as:

$$T_1 = \frac{a_f}{a}\sqrt{\frac{d_{\text{goal}}(a+a_o)}{2(a+a_f)(a_f-a_o)}}$$

$$T_2 = \sqrt{\frac{2d_{\text{goal}}(a+a_o)}{(a+a_f)(a_f-a_o)}}$$

$$T_3 = \sqrt{\frac{2d_{\text{goal}}(a_f-a_o)}{(a+a_f)(a+a_o)}}. \tag{5}$$

D. Iterative Error Reduction

Following the execution of a planned repositioning trajectory, there will be some error in the actual relative displacement due to trajectory tracking error, errors in initial conditions, or unmodeled dynamics. A significant source of error is an incorrect estimate of the friction coefficient μ. The following theorem shows that iterated executions of motion plans based on updated displacement information are sufficient to bring the object to the desired goal position d_{goal} in the presence of significant uncertainty in the friction coefficient.

Theorem 1: Consider the 1-DOF sliding regrasp system with a desired net sliding distance d_{goal}, a known constant normal force f_N, an estimated friction coefficient μ_0, and an actual (unknown) constant friction coefficient $\mu \in [\mu_0(1-\epsilon), \mu_0(1+\epsilon)]$ for a friction coefficient uncertainty $0 < \epsilon < 2/3$.

For any acceleration a in the range $\mu_0 f_N(2\epsilon - 1) < a < \mu_0 f_N(1-\epsilon)$, and for any positive constant ρ satisfying $\frac{\mu_0 f_N \epsilon}{a+\mu_0 f_N(1-\epsilon)} < \rho < 1$, by iterating the finger motion described in Section III-C (where d_{goal} is recalculated at each iteration based on perfect sensor data), the error in the net sliding distance converges exponentially to zero at least as fast as ρ^k converges to zero as the iteration number k goes to infinity, provided

$$a_f \geq \frac{\mu_0 f_N[\mu_0 f_N(1-\epsilon) + a(\epsilon/\rho + 1)]}{a - \mu_0 f_N[\epsilon(1+1/\rho) - 1]}.$$

Proof: See Appendix A.

Remark: From the condition on a_f given in Theorem 1, as the chosen value of ρ gets smaller, the required minimum value of a_f increases to ensure the convergence property.

The following example shows how choices of a, ρ, and a_f affect the iterative reduction algorithm. For a given $a_o > 0$ and $\epsilon = 0.2$, we choose $a = 0.4a_o$. The feasible range of ρ is $0.167 < \rho < 1$ according to the ρ constraints from Theorem 1. Note that the value of ρ determines the basic error convergence rate, and also affects the lower bound of the maximum finger acceleration a_f.

In practice, the choice of ρ and a_f should be based on manipulator acceleration constraints. Choosing $\rho = 0.5$ requires a finger acceleration a_f to be at least $1.7a_0$ to ensure that the error can be driven to zero at the rate ρ^k. Fig. 5 illustrates

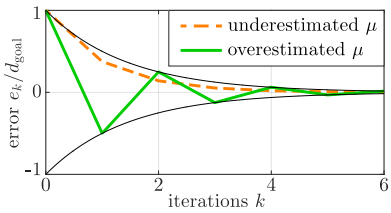

Fig. 5. Iterative reduction of the net error in sliding distance. The worst-case scenarios are shown, in which the actual friction coefficient is at the extreme $\mu = \mu_0(1-\epsilon)$ and $\mu_0(1+\epsilon)$. The solid black curves show the bounding convergence rate $\pm\rho^k$.

how the net sliding distance error converges to zero by iterating the motion planning in worst-case scenarios $\mu = \mu_0(1-\epsilon)$ and $\mu = \mu_0(1+\epsilon)$.

IV. General Problem Statement

In this section, we generalize the in-hand manipulation problem outlined in Section III to an n-fingered grasp, and define notation used in the rest of the paper.

We assume the object to be a laminar part that moves in a plane, held by n patch-contact fingers located on opposite sides of the part. The laminar part, and all motion of the part, are in a plane fixed at an angle α relative to a horizontal plane orthogonal to the gravity direction. A fixed frame $\mathcal{W}$ is defined in the plane of motion such that its x- and y-axes are basis vectors for the plane of motion and the y-axis is opposite to the projection of the gravity vector to the motion plane $\mathbf{g}_{\|} = [0, -mg\sin\alpha]^T$, as shown in Fig. 6.

The mass of the object is denoted by m, and its scalar inertia about its CM is I. The sum of out-of-plane forces applied to the object satisfies force balance at all instances so the object remains in the xy-plane of frame $\mathcal{W}$. We assume we can control the acceleration of each finger.

Frame $\mathcal{B}$ is the body frame fixed to the CM of the object, and the $x^{\mathcal{B}}$ and $y^{\mathcal{B}}$ axes are in the plane of the object. The finger contact patches are assumed circular. The frame $\mathcal{F}_i$ of the ith finger is located at the center of the finger's contact patch. We denote $\mathcal{B}^+$ and $\mathcal{F}_i^+$ as frames where the origins are coincident with $\mathcal{B}$ and $\mathcal{F}_i$, respectively, and the axes are aligned with $\mathcal{W}$. All configurations and velocities are defined with respect to the world frame $\mathcal{W}$ unless noted otherwise. All vectors are written in bold lowercase letters, all matrices are written in bold capital letters, and scalars are written in italic letters. We denote the configuration of the object by its pose $\mathbf{q}_o = [x, y, \theta]^T$, representing the position and orientation of $\mathcal{B}$ relative to $\mathcal{W}$. The location of the frame $\mathcal{F}_i$ is $\mathbf{q}_{fi} = [x_{fi}, y_{fi}, \theta_{fi}]^T$, and the entire n-fingered grasp is defined as $\mathbf{q}_f = [\mathbf{q}_{f1}^T, \ldots, \mathbf{q}_{fn}^T]^T$. The relative positions between the object and the finger contacts are defined as $\mathbf{r}_{fi} = [x_{rfi}, y_{rfi}, \theta_{rfi}]^T$, where $\mathbf{q}_{fi} = \mathbf{q}_o + \mathbf{r}_{fi}$, and the relative position for the entire grasp is defined as $\mathbf{r}_f = [\mathbf{r}_{f1}^T, \ldots, \mathbf{r}_{fn}^T]^T$. The configuration and velocity of the system are denoted as $\mathbf{q} = [\mathbf{q}_o^T, \mathbf{q}_f^T]^T$ and $\dot{\mathbf{q}} = [\dot{\mathbf{q}}_o^T, \dot{\mathbf{q}}_f^T]^T$. The full state of the system is defined as $[\mathbf{q}^T, \dot{\mathbf{q}}^T]^T$. Fig. 6 shows an example of a planar system with a rectangular object and patch contact fingers.

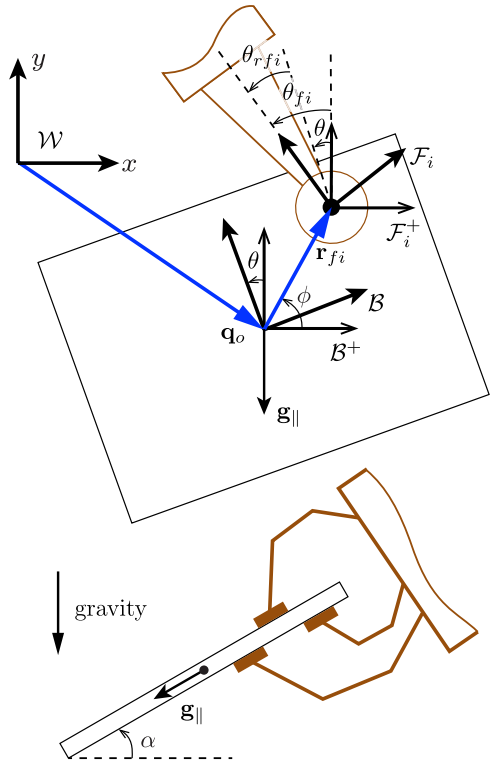

Fig. 6. Laminar object grasped by n patch contact fingers. (Top) View of the system in the object plane. The variables are defined in Section IV. (Bottom) The angle between the object plane and the horizontal plane is denoted as α.

V. Frictional Limit Surfaces

In this section, we discuss the concept of frictional limit surfaces (LS) and how they are shaped given circular patch contacts. Additionally, we derive expressions for the frictional force applied to the object from a patch contact with a given finger velocity relative to the object, and for the grasp limit surface given n individual limit surfaces.

A. Patch Contact

In this paper, friction is assumed to conform to Coulomb's law. For a circular patch contact, we denote $\mathbf{f} = [f_x, f_y, m_z]^T$ as the frictional wrench applied to the object expressed in frame $\mathcal{F}^+$. To describe the boundary of the frictional wrenches given the contact normal force, we use the concept of a frictional limit surface [22]–[24]. Frictional limit surfaces are convex and closed. When the frictional wrench $\mathbf{f}$ lies within the LS, the finger sticks on the object; and if the finger slides with velocity $\mathbf{v}$ relative to the object, the frictional wrench $\mathbf{f}_c$ is on the LS at a location where $\mathbf{v}$ is normal to the LS at $\mathbf{f}_c$ to satisfy the maximum work inequality (see Fig. 7).

The LS for a soft-finger contact can be approximated by an ellipsoid in the local frame [25]. A mathematical representation of the LS is given by the following quadratic form expressed in a local frame $\mathcal{F}^+$:

$$\mathbf{f}^T\mathbf{A}\mathbf{f} = 1 \tag{6}$$

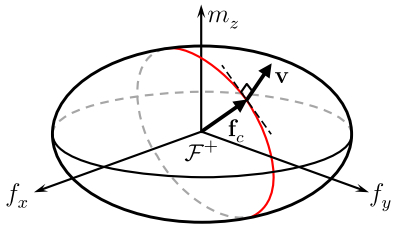

Fig. 7. Ellipsoid limit surface expressed in a local frame $\mathcal{F}^+$ attached to the center of the contact. The sliding direction $\mathbf{v}$ is along the normal of the ellipsoid at the corresponding frictional wrench $\mathbf{f}_c$.

where the matrix $\mathbf{A} \in \mathbb{R}^{3\times3}$ is a symmetric positive-definite matrix that determines the shape of the LS ellipsoid.

During sliding, the frictional wrench $\mathbf{f}_c$ lies on the LS, and we can write the relative velocity $\mathbf{v}$ along the direction of the gradient of the ellipsoid with respect to $\mathbf{f}$ at $\mathbf{f}_c$ as

$$\mathbf{v} = \lambda \left.\frac{\partial}{\partial \mathbf{f}}\left(\mathbf{f}^T \mathbf{A}\mathbf{f}\right)\right|_{\mathbf{f}_c} \tag{7}$$

for some $\lambda \in \mathbb{R}$, which scales the normal vector to the relative velocity vector. For a given relative velocity, the corresponding frictional wrench can be written as

$$\mathbf{f}_c = \frac{1}{\lambda}\mathbf{B}\mathbf{v} \tag{8}$$

where $\mathbf{B} = \frac{1}{2}\mathbf{A}^{-1}$. Substituting (8) into (6) and utilizing $(\mathbf{A}^{-1})^T = \mathbf{A}^{-1}$, we have

$$\lambda = \frac{1}{2}\sqrt{\mathbf{v}^T \mathbf{A}^{-1}\mathbf{v}}. \tag{9}$$

Combining (8) and (9), we derive the function $\Gamma(\cdot)$, which gives the frictional wrench as a function of a given relative velocity $\mathbf{v}$

$$\mathbf{f}_c = \Gamma(\mathbf{v}) = \frac{\mathbf{A}^{-1}\mathbf{v}}{\sqrt{\mathbf{v}^T \mathbf{A}^{-1}\mathbf{v}}}. \tag{10}$$

B. Grasp Limit Surface

When multiple fingers contact an object, the individual LS can be mapped to a common frame to generate the grasp limit surface (GLS). Let $\mathbf{f}_i$ represent the frictional wrench applied to the object expressed in the local frame $\mathcal{F}_i^+$. A reasonable choice of a common frame is the frame $\mathcal{B}^+$. The 3×3 matrix $\mathbf{G}(\mathbf{r}_{fi})$ is the map relating the frictional wrench $\mathbf{f}_i$ in $\mathcal{F}_i^+$ to the wrench expressed in $\mathcal{B}^+$. Matrices $\mathbf{G}(\mathbf{r}_{fi})$ depend on the contact position relative to the object CM and is defined as

$$\mathbf{G}(\mathbf{r}_{fi}) = \mathbf{G}_i = \begin{bmatrix} 1 & 0 & 0 \\ 0 & 1 & 0 \\ -y_{rfi} & x_{rfi} & 1 \end{bmatrix}. \tag{11}$$

The grasp limit surface is the convex hull of the sum of all possible friction forces that the grasp can resist. The GLS can be expressed in $\mathcal{B}^+$ as

$$GLS = \delta\left\{\mathbf{f} | \mathbf{f} = \sum_{i=1}^{n} \mathbf{G}_i \mathbf{f}_i \,\forall\, \mathbf{f}_i \in LS_i\right\} \tag{12}$$

where δ is an operator that takes the boundary of the set, $\mathbf{f} = [f_x, f_y, m_z]^T$ is an arbitrary friction force on the GLS, and LS_i is the limit surface for contact i.

Fig. 8 shows an example of a four-fingered grasp on an object and the resulting limit surfaces with frictional torques about the corresponding contact center, transferred frictional torques expressed in $\mathcal{B}^+$, and the combined grasp limit surface.

VI. Dynamics

In this section, we derive the dynamics for the case where the object is sticking and when it is sliding. We assume that the system state $[\mathbf{q}^T, \dot{\mathbf{q}}^T]^T$, the matrices $\mathbf{A}_i$ that determine the shape of LS_i, and either the desired relative finger accelerations $\ddot{\mathbf{r}}_{fi}(t)$ or the finger accelerations $\ddot{\mathbf{q}}_{fi}(t)$ are given.

A. Sticking Dynamics

The object's dynamics are defined as

$$\mathbf{M}\ddot{\mathbf{q}}_o = \sum_{i=1}^{n} \mathbf{G}_i \mathbf{f}_i + \mathbf{g} \tag{13}$$

where $\mathbf{M} = \mathrm{diag}(m, m, I)$ is the mass matrix of the object and $\mathbf{g} = [0, -mg\sin\alpha, 0]^T$ is the wrench on the object due to gravity in the object plane expressed in frame $\mathcal{B}^+$. For the sticking case, the frictional force at each contact is contained within the limit surface, i.e., $\mathbf{f}_i^T \mathbf{A}_i \mathbf{f}_i < 1$.

B. Sliding Dynamics

During sliding, relative velocity at each contact is defined as

$$\mathbf{v}_i = \dot{\mathbf{q}}_{fi} - \mathbf{G}_i^T \dot{\mathbf{q}}_o. \tag{14}$$

The forward dynamics problem is to determine the relative acceleration of each finger $\ddot{\mathbf{r}}_{fi}$ when given the state of the system $[\mathbf{q}, \dot{\mathbf{q}}]^T$, the LS_i shape matrices $\mathbf{A}_i$, and the accelerations of each finger $\ddot{\mathbf{q}}_{fi}$. First, we define the relative acceleration as

$$\ddot{\mathbf{r}}_{fi} = \ddot{\mathbf{q}}_{fi} - \ddot{\mathbf{q}}_o. \tag{15}$$

The dynamics in (13) can be rewritten as

$$\ddot{\mathbf{q}}_o = \mathbf{M}^{-1}\left[\sum_{i=1}^{n} \mathbf{G}_i \mathbf{f}_i + \mathbf{g}\right]. \tag{16}$$

Combining (10), (14), (15), and (16), we can write the relative finger acceleration as

$$\ddot{\mathbf{r}}_{fi} = \ddot{\mathbf{q}}_{fi} - \mathbf{M}^{-1}\left[\sum_{i=1}^{n} \mathbf{G}_i \Gamma(\dot{\mathbf{q}}_{fi} - \mathbf{G}_i^T \dot{\mathbf{q}}_o) + \mathbf{g}\right]. \tag{17}$$

This equation allows us to calculate the relative sliding motion for given finger accelerations, and solves the forward dynamics problem.

The inverse problem is trivial, and (17) can easily be rearranged to solve for the required finger accelerations when given a desired relative sliding motion. For the inverse problem, it is more convenient to give the relative acceleration w.r.t. the body frame as the input. Denoting $\ddot{\mathbf{r}}_{fi}^{\mathcal{B}}$ as the relative acceleration

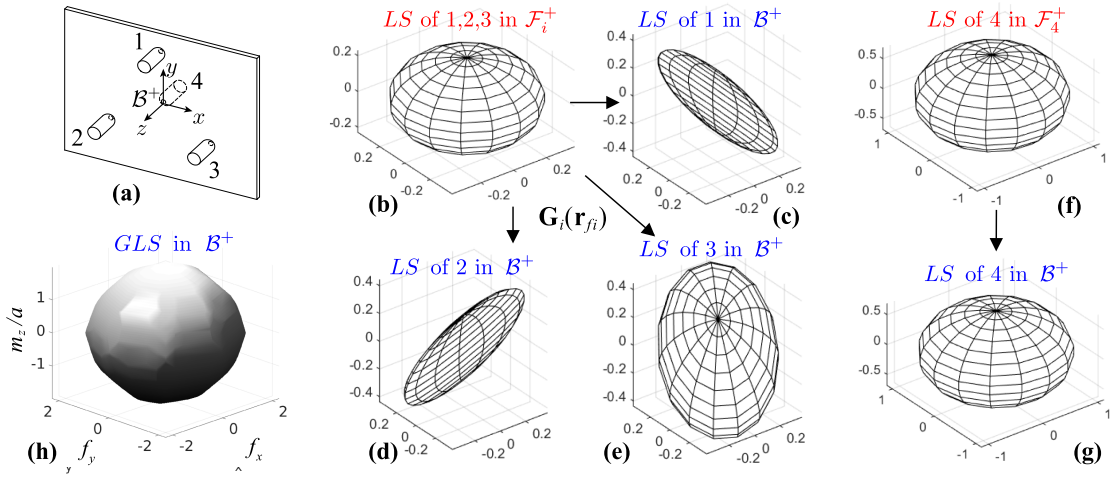

Fig. 8. Four-fingered grasp and the resulting limit surfaces in the local finger frames, the body frame, and the composite grasp limit surface. (a) Sketch of the grasp with three fingers on one side and one on the opposite side. (b) Identical limit surface for fingers 1–3 in the local finger frames $\mathcal{F}_i^+$. (c)–(e) Limit surfaces from fingers 1, 2, and 3, respectively, mapped to the common frame $\mathcal{B}^+$ using the $\mathbf{G}_i$ transformation. (f) Limit surface for finger 4, which is the same in $\mathcal{F}_4^+$ as $\mathcal{B}^+$ since they are coincident. (h) Composite grasp limit surface. The axes in (b)–(g) are all aligned and equivalent to the axes in (h).

w.r.t. the body frame $\mathcal{B}$, we have

$$\mathbf{r}_{fi} = \mathbf{T}_i(\theta)\mathbf{r}_{fi}^{\mathcal{B}} \tag{18}$$

where $\mathbf{T}_i(\theta) \in SE(2)$ is the homogeneous transformation that maps $\mathbf{r}_{fi}^{\mathcal{B}}$ into $\mathbf{r}_{fi}$

$$\mathbf{T}_i(\theta) = \begin{bmatrix} \cos\theta & -\sin\theta & 0 \\ \sin\theta & \cos\theta & 0 \\ 0 & 0 & 1 \end{bmatrix}.$$

Taking the first and second derivative with respect to time on both sides of (18) gives

$$\dot{\mathbf{r}}_{fi} = \dot{\mathbf{T}}_i\mathbf{r}_{fi}^{\mathcal{B}} + \mathbf{T}_i\dot{\mathbf{r}}_{fi}^{\mathcal{B}} \tag{19}$$

$$\ddot{\mathbf{r}}_{fi} = \ddot{\mathbf{T}}_i\mathbf{r}_{fi}^{\mathcal{B}} + 2\dot{\mathbf{T}}_i\dot{\mathbf{r}}_{fi}^{\mathcal{B}} + \mathbf{T}_i\ddot{\mathbf{r}}_{fi}^{\mathcal{B}}. \tag{20}$$

VII. Motion Planning

In this section, we focus on motion planning to achieve a desired sliding regrasp. For simplicity, we assume that each finger of the hand remains stationary relative to the palm of the hand, so we only plan the motion of the three degrees of freedom of the palm, not individual motions of the fingers.

The motion planning problem can be stated as: given an initial grasp of the object and a desired relative configuration between the object and the hand, find a motion of the hand that achieves this reconfiguration by dynamic in-hand sliding.

The details of the grasp limit surface, and therefore the sliding dynamics, are a function of the number of fingers, their placement on the object, and the normal force control strategy. A specific type of grasp, a two-fingered pinch grasp, is examined in Section VIII and used in our experiments.

A. Specifications for the Motion Planner

1) The grasp limit surface details for the specific grasp are given.
2) The hand motion yields a sticking phase, followed by a sliding phase, followed by a sticking phase. The time periods for each phase are denoted T_1, T_2, and T_3, respectively, and the total time is denoted $T_{\text{total}} = T_1 + T_2 + T_3$.
3) From the given initial grasp and desired relative configuration, the initial and goal relative positions between the object and the fingers $\mathbf{r}_{f,\text{init}}^{\mathcal{B}}$ and $\mathbf{r}_{f,\text{goal}}^{\mathcal{B}}$ can be calculated and are inputs to the motion planner.
4) The relative finger trajectory $\mathbf{r}_f^{\mathcal{B}}(t)$ in the sliding phase and object trajectories $\mathbf{q}_o(t)$ in the sticking phases are defined as cubic polynomials of time, in which each motion component is of the form $a_0 + a_1 t + a_2 t^2 + a_3 t^3$, defined by four coefficients. Thus, the start and end position and also velocity provide four constraints on the four coefficients, uniquely defining the polynomial as a function of time.
5) The system starts and ends at rest with no relative velocity between the part and object, so $\dot{\mathbf{q}}_o(0) = 0$, $\dot{\mathbf{q}}_o(T_{\text{total}}) = 0$, $\dot{\mathbf{r}}_f^{\mathcal{B}}(T_1) = 0$, $\dot{\mathbf{r}}_f^{\mathcal{B}}(T_1 + T_2) = 0$.

B. Planning Algorithm

With the specifications above, the hand and object motion is determined by a set of design variables. The system motion is split into three phases: sticking, sliding, and sticking. In the first sticking phase, we have to choose the object start configuration (initial velocity is zero), end configuration, end velocity, and duration ($3 + 3 + 3 + 1 = 10$ design variables). For the sliding phase, we have to choose only the duration of sliding (one design variable). For the second sticking phase, we have to specify the final object configuration and the duration of the phase ($3 + 1 = 4$ design variables). Thus, there is a total of 15 design variables defining a motion plan. As described below, the motion planning problem is turned into a nonlinear root-finding problem to find these 15 variables.

We denote t as the time variable for the entire motion, $t \in [0, T_{\text{total}}]$, and t_i as the time variable for each phase starting at

zero and ending at the duration of that phase, $t_i \in [0, T_i]$, $i = 1, 2, 3$. The details of the design variables and constraints on each phase are given below.

1) First Sticking Phase: The design variables are $\mathbf{q}_o(0), \mathbf{q}_o(T_1), \dot{\mathbf{q}}_o(T_1)$, and T_1. The use of cubic polynomials means there are no freedoms in the trajectory shapes once the boundary conditions are set. Therefore, $\mathbf{q}_o(t_1)$ is determined with a given set of the ten design variables. Note that because the initial relative position is not relevant to where the object is in the world frame, we can choose any initial position $\mathbf{q}_o(0)$. The frictional wrench $\mathbf{f}_i(t_1)$ can be calculated by the sticking dynamics discussed in Section VI-A. Since there is no relative motion in the sticking phase, the finger motions $\mathbf{q}_{fi}(t_1)$ are determined as long as $\mathbf{q}_o(t_1)$ and the relative positions $\mathbf{r}^{\mathcal{B}}_{f,\text{init}}$ are given.

The constraints that have to be satisfied are manipulator constraints (including workspace, velocity, and acceleration limits) and that the frictional wrenches are always inside the limit surfaces during the first sticking phase.

2) Sliding Phase: The design variable is T_2. In the sliding phase, the cubic polynomial defining the object motion relative to the hand is fully specified by $\mathbf{r}^{\mathcal{B}}_{f,\text{init}}$ and $\mathbf{r}^{\mathcal{B}}_{f,\text{goal}}$, which are given. The initial state of the hand is given by the design variables $\mathbf{q}_o(T_1)$ and $\dot{\mathbf{q}}_o(T_1)$ from the first sticking phase above. To find the hand motion during this sliding phase, we first solve the inverse dynamics using the hand state at the beginning of the trajectory, as well as $\ddot{\mathbf{r}}^{\mathcal{B}}_f$, to find the hand acceleration $\ddot{\mathbf{q}}_f$. Taking a small integration step, we get the next state of the hand, solve the inverse dynamics again, etc., until we have numerically constructed the trajectory of the hand during the sliding phase based on the initial state of the hand and the prespecified relative object motion during sliding.

The constraints that have to be satisfied in the sliding phase are manipulator constraints.

3) Second Sticking Phase: The design variables are $\mathbf{q}_o(T_{\text{total}})$ and T_3. Similar to the first sticking phase, the hand motion $\mathbf{q}_{fi}(t_3)$ and object motion $\mathbf{q}_o(t_3)$ are determined by the specified final conditions and the initial conditions $\mathbf{q}(T_1 + T_2)$ and $\dot{\mathbf{q}}(T_1 + T_2)$ from the final state of the sliding phase.

The constraints that have to be satisfied are manipulator constraints and that the frictional wrenches are always inside the limit surfaces during the second sticking phase.

4) Full Motion Planning Problem Statement:

$$\begin{aligned}
&\textbf{given} && \mathbf{r}^{\mathcal{B}}_{f,\text{init}}, \mathbf{r}^{\mathcal{B}}_{f,\text{goal}} \\
&\textbf{find} && T_1, T_2, T_3,\ \mathbf{q}_o(0),\ \mathbf{q}_o(T_{\text{total}}),\ \mathbf{q}_o(T_1),\ \dot{\mathbf{q}}_o(T_1) \\
&\textbf{such that} && \mathbf{r}^{\mathcal{B}}_f(T_1) - \mathbf{r}^{\mathcal{B}}_{f,\text{init}} = 0, \\
& && \mathbf{r}^{\mathcal{B}}_f(T_1 + T_2) - \mathbf{r}^{\mathcal{B}}_{f,\text{goal}} = 0, \\
& && \text{and the dynamics of each phase} \\
& && \text{and manipulator constraints are satisfied.}
\end{aligned}$$

This is a multidimensional root-finding problem with constraints, and we use MATLAB's `fmincon` SQP solver to solve it. An initial guess of the design variables is automatically generated based on heuristics encoding our knowledge of the task.

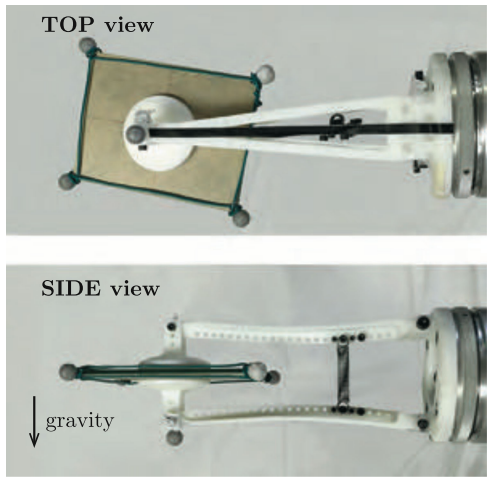

Fig. 9. Lightweight, spring-powered, constant-gripping-force gripper.

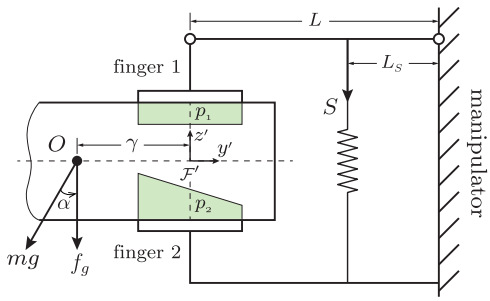

Fig. 10. Side view of the system. The green shaded regions show the pressure distributions of the contacts.

VIII. Limit Surfaces for a Pinch Grasp

The modeling and motion planning of the previous sections require the individual fingertip limit surfaces as a function of the configuration of the object relative to the hand, and these limit surfaces depend on the specifics of the grasp. In this paper, we focus on a two-fingered pinch grasp with fingertip patch contacts. To focus on the essential ideas of this paper, the mechanics of sliding regrasp, and iterative motion planning and execution, we built a custom two-fingered passive gripper, shown in Fig. 9. We use this gripper instead of the Allegro hand for two reasons: 1) it is lighter than the Allegro hand (0.25 kg versus 1.2 kg), which allows larger accelerations, and 2) it creates a well-characterized constant normal force at the fingertips, allowing us to avoid the potential confounding issue of errors in fingertip force control while we validate the general approach.

In this section, we describe the contact model of the constant-gripping-force gripper, and in Section IX we describe regrasp experiments using it.

A. Pinch–Grasp Description

For this analysis, we focus on the case of a zero-thickness planar object pinched by two fingers on opposite sides of the part (see Fig. 10). The two fingers stay stationary relative to each other, and we assume circular contact patches with the

same fixed radius a. The plane in which the object and the manipulator move is tilted by angle α from the horizontal plane as shown in Fig. 6. We denote $f_g = -mg\cos\alpha$ as the gravity force acting on the object in the out-of-plane direction.

Finger 1, on the top of the object, is connected to the manipulator by two hinges and an arm of length L. Finger 2, on the bottom of the object, is connected to the manipulator through an arm fixed to the manipulator with the same length L. The two hinges keep the two flat circular fingers parallel to each other and in full contact with the object. The distance from the hinges to the contact of finger 1 is assumed to be zero. The spring is located L_S away from the manipulator and the spring force is denoted S. This model allows us to control the normal forces at the fingers by the spring stiffness (another model could be force control of the manipulator in the normal direction and motion control in the two linear tangent directions and rotation about the contact normal).

B. Fingertip Limit Surfaces

We first note four important features of the two-fingered pinch grasp:

1) *Collocated Point Fingers Cannot Hold the Object:* Remembering that the laminar object is modeled in the limit of zero thickness, the contact point of each finger would be at the same point. Therefore, contact forces from the two collocated fingertips always make zero moment about the contact point, and they cannot balance the moment due to gravity. This issue can be addressed by having contact patches instead of point contacts.
2) *Pressure Distribution at a Contact Patch is Generally Unknowable:* If the object and fingertip are modeled as rigid bodies, then the pressure as a function of the location on a continuous contact patch will be indeterminate. Our approach is to use the simplest possible model of the pressure distribution that is physically consistent, and to account for any unknowable modeling errors by iterative regrasping.
3) *Simplest Pressure Distribution, Uniform Pressure, is Physically Inconsistent:* If both contact patches have a uniform pressure distribution, then the two design variables available (the pressure at each patch) are insufficient to provide force–moment balance of the object in gravity.
4) *Lowest Order Physically Consistent Pressure Distribution Model is Uniform Pressure on Finger 1 and Linearly Varying Pressure on Finger 2:* The uniform pressure on finger 1 assures that the total normal force passes through the rotational joint above the finger. The linearly varying pressure distribution on finger 2 provides the extra variable needed to solve uniquely for the pressure distributions while assuring that the object remains in the plane of motion.

Fig. 10 illustrates the two contact pressure distributions, viewed from the side. The pressure p_1 is constant over the contact patch, modeled as a disk of radius a. The pressure p_2 is also defined over a disk of radius a. Defining a y' axis as the axis from the center of mass of the object to the center of the contact disk, the pressure distribution varies linearly along y' and is constant along the orthogonal direction (see (29) in Appendix B for the expression of p_2). As shown in Fig. 10, to maintain a static grasp, p_2 is more closer to the center of mass and drops with increasing y'. This allows for force and moment balance considering the gravity force on the object.

Let γ be the distance from the object center of mass to the center of the finger contact patches. As shown in Appendix B, the minimum spring force S needed to maintain the grasp increases as γ increases, according to

$$S \geq \frac{f_g L}{L_S}\left(\frac{4\gamma}{a} - 1\right). \tag{21}$$

For a spring force less than this bound, the required pressure p_2 for force–moment balance becomes negative within finger 2's contact patch, which is not physically realizable. Therefore, moment balance cannot be achieved, and the object rotates and falls out of the plane of motion. You can try a simple experiment with a cell phone to see that a larger grip force is needed to hold the phone horizontal as the pinching fingers move further from the center of mass.

Based on the modeling above, Appendix B derives the detailed forms of the limit surfaces describing the contacts at finger 1 and finger 2. The limit surfaces are based on ellipsoidal approximations to the elliptic integrals corresponding to the finger contact forces and moments. The resulting closed-form expressions are $\mathbf{f}_i^T \mathbf{A}_i \mathbf{f}_i = 1$, where for finger 1 $\mathbf{A}_1 = \mathbf{A}(0)$ and for finger 2 $\mathbf{A}_2 = \mathbf{A}(\gamma)$. The expression for $\mathbf{A}(\gamma)$ can be found in (52) in Appendix B.

With the description of the contact limit surfaces as a function of the configuration of the object in the hand, we apply the dynamics and motion planning described in Sections V–VII to experiments.

TABLE I
LIMITS FOR MANIPULATOR JOINT VELOCITIES AND ACCELERATIONS

joint #	$\dot{\Theta}_{\min}$ (rad/s)	$\dot{\Theta}_{\max}$ (rad/s)	$\ddot{\Theta}_{\min}$ (rad/s^2)	$\ddot{\Theta}_{\max}$ (rad/s^2)
1	-2	2	-12	12
4	-5	5	-80	80
6	-20	20	-100	100

TABLE II
PARAMETER VALUES FOR THE TWO-FINGERED GRASP SYSTEM

object mass m	0.049 kg
object dimensions	0.12 m $\times$ 0.09 m
object inertia I (about its CM)	2.78×10^{-4} kg·m^2
angle between the horizontal plane α	0
gravity constant g	9.8 m/s^2
gripper arm length L	0.17 m
spring location L_S (as shown in Fig. 10)	0.05 m
spring load S	-7 N
measured friction coefficient $\hat{\mu}$	0.34
friction coefficient used in planning μ	0.16
radius of the contact patch a	0.0254 m
3R robot link 1 length	0.552 m
3R robot link 2 length	0.303 m
3R robot link 3 length	0.287 m

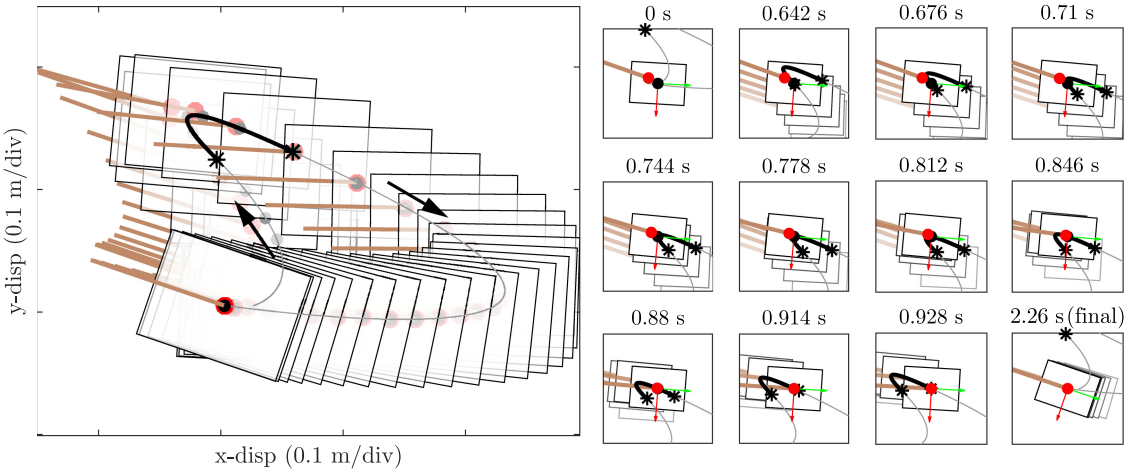

Fig. 11. *Repositioning example:* showing trajectories found by the motion planner. The plot on the left shows the entire motion with a time interval between frames of 60 ms. Plots on the right show the initial and final configurations, and give more details of motion during the sliding phase. Solid gray curves are the object CM trajectories, red dots represent the finger contacts, and the brown lines represent the finger orientation. Thick black arrows show the directions of the object motion. Thick black curves show the sliding regions. Thin red and green arrows are the x and y directions of the body frame $\mathcal{B}$.

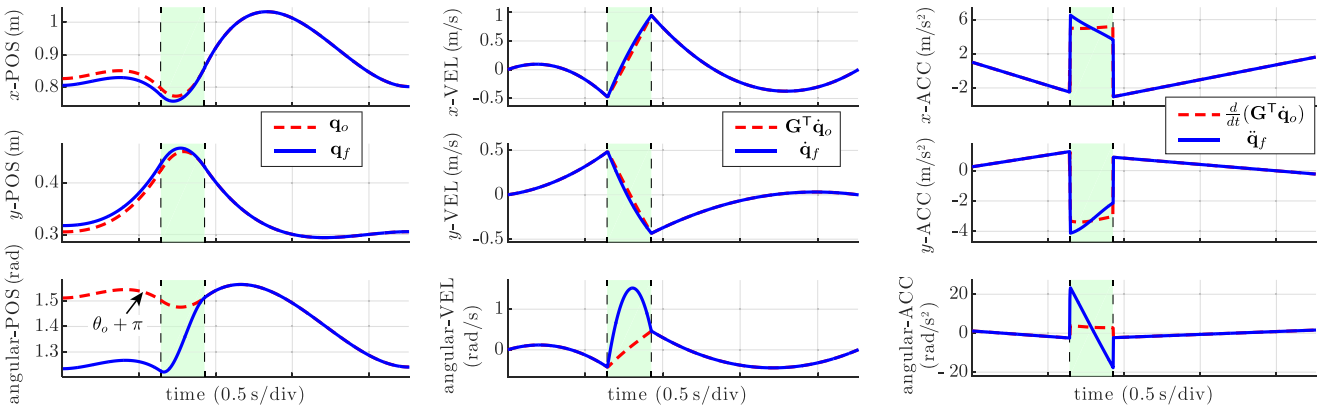

Fig. 12. *Repositioning example:* showing the trajectories of the object (red dashed curves) and the finger (blue solid curves) found by the motion planner to reposition an object. Green shaded regions show the planned sliding phase. (Left) Finger contact center trajectories $\mathbf{q}_f$ and object CM trajectories $\mathbf{q}_o$. Initial relative position error is shown as the space between the dashed red line and the blue line, which is reduced to zero after the sliding motion. (Middle) Finger velocities $\dot{\mathbf{q}}_f$ and object contact points velocities (points on the object that are coincident with the contact center) $\mathbf{G}^T\dot{\mathbf{q}}_o$ are shown to demonstrate relative velocities at the contact. (Right) Finger accelerations $\ddot{\mathbf{q}}_f$ and object contact point accelerations $\frac{d}{dt}(\mathbf{G}^T\dot{\mathbf{q}}_o)$ demonstrate relative accelerations at the contact.

IX. Experiment

We tested the motion planner discussed in Section VII with a pinch–grasp introduced in Section VIII using the ERIN system described in Section I-A.

We used the lightweight passive gripper rather than the Allegro hand for the higher achievable accelerations and better contact force characterization as discussed in the beginning of Section VIII. We used three joints of the 7-DOF WAM arm (joints 1, 4, and 6) while keeping the other joints fixed to emulate a 3R planar arm. Manipulator workspace, velocity, and acceleration constraints in the root-finding problem were based on joint, velocity, and motor properties given by the manufacturer as well as conservative estimates of the inertia matrix. The values of manipulator velocity and acceleration constraints are shown in Table I.

Given initial and goal relative configurations, the motion planner plans the hand trajectory and solves the joint trajectories using inverse kinematics. The planned joint trajectories were generated offline, and real-time control was used to follow the trajectories specified by the planner. The motion control loop used encoder feedback and ran at 500 Hz on a Linux PC with an Intel Core i7-4770 CPU and 16 GB RAM. Motion was in a horizontal plane ($\alpha = 0$) to achieve more isotropic control authority than would be the case in a vertical plane. The values of the constants used in modeling and planning are summarized in Table II.

A. One-Shot Planning and Execution

Before planning, the initial relative position $\mathbf{r}^{\mathcal{B}}_{f,\text{init}}$ was measured by the vision system. With the goal relative position $\mathbf{r}^{\mathcal{B}}_{f,\text{goal}}$

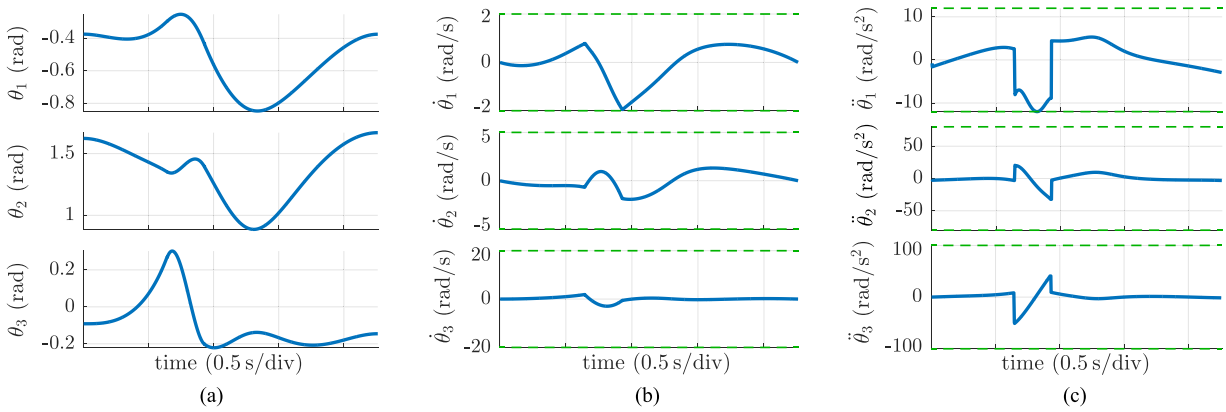

Fig. 13. *Repositioning example:* blue curves showing the planned joint positions, velocities, and accelerations of the manipulator calculated from the finger trajectories shown in Fig. 12 by solving inverse kinematics. The green dashed lines are the joint velocity and acceleration limits corresponding to the values in Table I. Joint position limits are not shown since the trajectories are far from the limits.

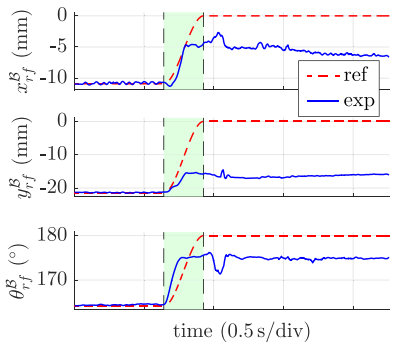

Fig. 14. Experiment result of one-shot planning showing the relative position changes versus time. Red dashed curves show the reference relative position $\mathbf{r}_f^{\mathcal{B}}$ trajectories. Blue curves represent the actual relative position trajectories. Green shaded regions indicate the planned sliding phase.

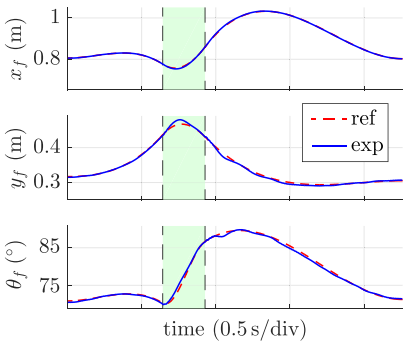

Fig. 15. Experiment result of one-shot planning, showing the finger contact center trajectories. Green shaded regions indicate the planned sliding phase. The mean absolute tracking errors are $[1.02\,\text{mm}, 2.56\,\text{mm}, 0.296\,^\circ]^T$, and the standard deviations are $[1.04\,\text{mm}, 2.75\,\text{mm}, 0.27\,^\circ]^T$.

given by the user, the motion planner calculated the motion of the robot to realize the repositioning satisfying all the constraints.

Figs. 11 and 12 show the motion planning result of a sliding regrasp example. The initial relative position was measured as $\mathbf{r}^{\mathcal{B}}_{f,\text{init}} = [-0.011\,\text{m}, -0.022\,\text{m}, 164^\circ]^T$, and the goal relative position was given as $\mathbf{r}^{\mathcal{B}}_{f,\text{goal}} = [0, 0, 180^\circ]^T$. Fig. 13 shows the planned joint trajectories of the 3R robot, which were calculated from the inverse kinematics applied to the finger position trajectories in Fig. 12. The planned time periods for each phase were $T_1 = 0.64$ s, $T_2 = 0.29$ s, and $T_3 = 1.33$ s.

The planned motions were tested experimentally. The WAM arm followed the preplanned joint trajectories using a PID-based joint position controller. The object poses were obtained from the vision system. To prevent overshoot during the sliding motion, we chose an underestimated friction coefficient in the motion planner. Experimental results of relative position change are shown in Fig. 14. Finger position tracking results are shown in Fig. 15, where the finger poses were calculated from the recorded joint angles and the forward kinematics of the system.

During the implementation, the finger moved relative to the object along the desired direction and ended up with some undershoot errors, which were more apparent in the y direction. One reason for this undershoot is the intentionally underestimated friction coefficient in the motion planner. Another reason is the trajectory tracking error is larger in the y direction as shown in Fig. 15. Since there is more error in the y direction from the initial configuration, the planned motion has higher accelerations in this direction, which increases the tracking error. The final relative position errors could also have been caused by modeling errors and uncertainties in measuring the initial relative positions.

B. Iterative Planning and Execution

This section reports the results of iterative planning and execution for 3-DOF planar regrasping. Unlike the idealized 1-DOF example in Section III, we have no theoretical convergence results for iterative in-hand regrasping for the 3-DOF case and all possible sources of error. The motivation for iterative regrasping (essentially discrete-time one-step deadbeat feedback control) is the same, however.

In each experiment, we tested three iterations of motion planning and execution with the same goal. In each iteration, the

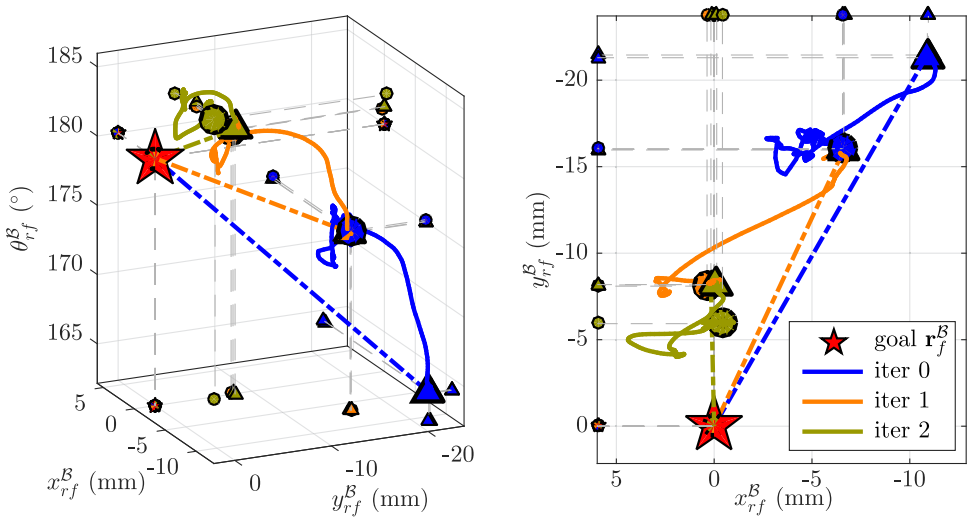

Fig. 16. Experimental results of iterative planning and execution for one experiment consisting of three iterations. The plots show the planned and actual relative configurations $\mathbf{r}^{\mathcal{B}}_{f}(t)$. Each color represents one iteration. Triangles and circles show the initial and final points of each trajectory. The dashed lines are the planned trajectories and the solid curves shows the experimental results. Plots on the left and right show the same result from different viewpoints.

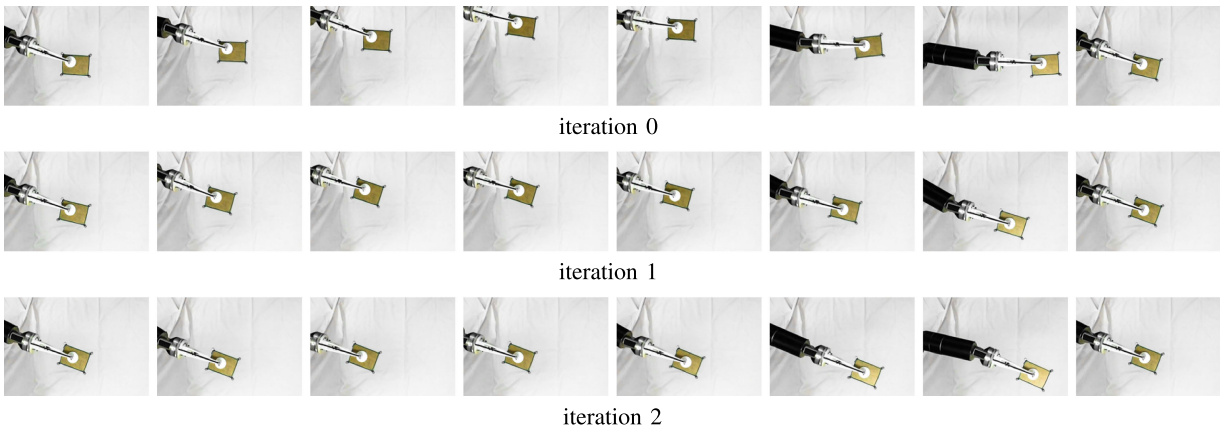

Fig. 17. Iterative planning experiment corresponding to Fig. 16. Total times for iterations 0, 1, and 2 are 2.26 s, 1.6 s, and 1.95 s, respectively. Time intervals between snapshots were manually chosen to show the motion of the system. A video of this experiment is shown in the attached media.

initial state was measured from the last state of the previous iteration. The robot trajectories were planned automatically by the motion planner based on the initial state and goal state. Then, the robot followed the planned trajectories.

Results of the iterative planning are shown in Figs. 16 and 17. The first iteration corresponds to the example given in Section IX-A. After each iteration, the relative position was closer to the goal configuration. Once the object is near the goal state, additional iterations did not decrease the error. In cases where the error was close to the mean vision error of the vision system ($\sim$0.5 mm), additional iterations could actually introduce more error.

C. Repeatability

To test the repeatability of the repositioning experiment, we ran the previous three-iteration experiment ten times, making a total of 30 motion plans and executions. At the beginning of each three-iteration trial, the object was manually placed at approximately the same initial configuration. Fig. 18 shows a boxplot of the relative position changes. Fig. 19 shows a boxplot of the planning time. Further iterations produce no statistically significant improvement (or worsening) of the grasp.

Sources of error in achieving planned regrasps include vision errors (as mentioned above), error in following the planned robot trajectory, and contact modeling errors (e.g., the Coulomb friction approximation and the contact pressure distribution approximations). The mean absolute robot trajectory tracking errors were $[1.2\,\text{mm}, 2.6\,\text{mm}, 0.35\,^\circ]^T$, with standard deviations $[0.91\,\text{mm}, 2.6\,\text{mm}, 0.22\,^\circ]^T$, respectively. Errors induced by the assumed form of the contact pressure distributions are likely less meaningful for n-fingered grasps than for our 2-fingered grasp, because the distances between the finger contacts play a larger role in determining the shape of the grasp limit surface than the detailed pressure distribution at single fingers. While our finger/object contacts approximately obeyed a dry Coulomb friction model, other finger/object contacts, particu-

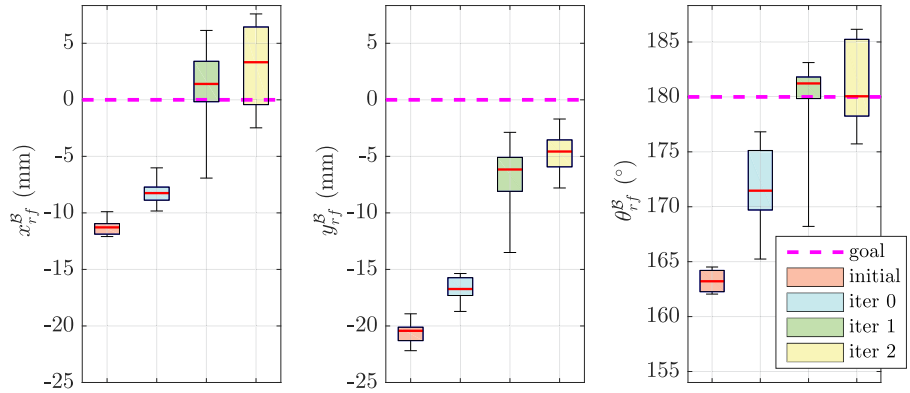

Fig. 18. Experiment results of ten trials, showing the changes of relative positions. Each color represents one iteration. The red lines within the boxes show the mean values, edges of the boxes are the 25th and 75th percentiles, and whiskers extend to the most extreme data points.

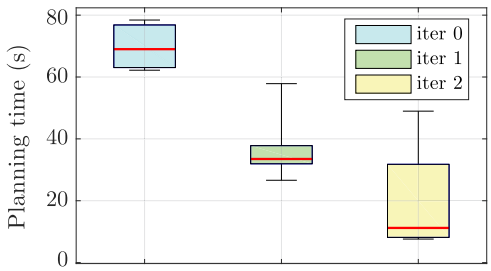

Fig. 19. Planning time of 10 trials. Each color represents one iteration. Red lines within the boxes show the mean values, edges of the boxes are the 25th and 75th percentiles, and whiskers extend to the most extreme data points.

larly involving soft, hysteretic materials such as rubber, may require a different contact model.

The goal configuration was the same in all 30 individual planning and execution steps, but the initial configurations varied considerably. The results of the reported experiments are in line with what we observed with other 3-DOF 2-fingered laminar regrasps we tried, and point to a typical final error on the order of a few millimeters in linear position and a few degrees in orientation. Achieving a smaller final error would require improvements in the vision system, trajectory tracking, or contact modeling.

X. Conclusion

In this paper, we presented a general framework for planning dynamic in-hand sliding manipulation motions and analyzed the dynamics for n-fingered grasps using soft-finger limit surface models. We proposed a simple model of the contact pressure distribution and constructed the frictional limit surfaces based on it. The framework was applied to the problem of in-hand sliding manipulation with a two-fingered grasp in the horizontal plane. Our motion planner was able to automatically find dynamic hand motions to achieve a desired sliding regrasp based on the grasp contact model. Experimental implementations of iterative planning and execution reduced the relative position error and demonstrated the feasibility of the overall approach.

Future work includes problems 5 and 6 from Section I-A: 5) real-time feedback control of finger motions and normal forces during the regrasp and 6) iterative improvement of the finger contact models using data from experiments. Problem 5 will likely require better fingertip force sensors and higher bandwidth fingertip force control than is currently available to us. Also, practical estimates are needed on the ultimate error after iterative regrasping, based on reasonable models of trajectory tracking capabilities and contact modeling uncertainties. For example, Theorem 1, which promises zero ultimate error for an idealized 1-DOF regrasping problem, is based on perfect trajectory tracking, perfect sensing, and a constant (though unknown) friction coefficient. Each of these assumptions should be weakened to better understand the importance of each factor. Our experiments indicate a practical ultimate error of a few millimeters.

This paper studied 3-DOF planar regrasping using a 2-fingered grasp on parallel surfaces. The method can easily be extended to n-fingered grasps on parallel surfaces by modifying the grasp pressure distribution details in Section VIII. Extensions to n-fingered regrasping on nonparallel surfaces requires adding compliance (or contact normal force control) at the individual fingers to allow finger compliance in the normal direction, which is a topic we are currently investigating.

Appendix A
Proof of Theorem 1

Proof: Without loss of generality, we prove the theorem for the case $d_{\text{goal}} > 0$, as indicated in Fig. 4. With friction uncertainty included, the friction coefficient is $\mu \in [\mu_0(1-\epsilon),\ \mu_0(1+\epsilon)]$. The object acceleration during sliding therefore satisfies $a_{o,\text{actual}} \in [a_o - a_\epsilon,\ a_o + a_\epsilon]$, where $a_o = \mu_0 f_N$ and $a_\epsilon = \mu_0 f_N \epsilon$.

To understand these conditions, we first discuss sliding distance error caused by the friction uncertainty. For the case when the friction coefficient is larger than the estimate, the object will undershoot d_{goal}. The maximum sliding distance error caused by the underestimated friction coefficient is the area of the dark orange triangle d_2 in Fig. 4, and

$$d_2 = \frac{(a + a_f)a_\epsilon d_{\text{goal}}}{(a_f - a_o)(a + a_o + a_\epsilon)}. \tag{22}$$

For the case where the actual friction coefficient is smaller than the estimate, the object will slide more than d_{goal}. The maximum sliding distance error is the area of the dark green triangle d_3 in Fig. 4, which can be expressed as

$$d_3 = \frac{(a + a_f)a_\epsilon d_{\text{goal}}}{(a_f - a_o)(a + a_o - a_\epsilon)}. \tag{23}$$

From (22) and (23), the maximum sliding distance errors satisfy $d_2 < d_3$ for any $a_f > a_o$ regardless of what a_f is chosen. Therefore, we focus on the conditions on d_3 to ensure that the sliding distance errors decrease within the given rate.

From (23), when $a_f > a_o$, and with given a_o and a_ϵ, as a_f increases to infinity d_3 converges to its minimum value of $\frac{a_\epsilon d_{\text{goal}}}{a + a_o - a_\epsilon}$. Although it initially seems counterintuitive, increasing the finger acceleration a_f decreases the overshoot error because the phase durations become smaller [see (5)]. To prevent the object from sliding too far, the condition $d_3 < d_{\text{goal}}$ should be ensured. Therefore, we have a lower bound for a:

$$\frac{a_\epsilon}{a + a_o - a_\epsilon} < 1 \;\Rightarrow\; a > \mu_0 f_N (2\epsilon - 1).$$

An upper bound on a ensures that the object sticks in the beginning and end modes when the friction is overestimated, and is expressed by $a < \mu_0 f_N (1 - \epsilon)$. To ensure a feasible a exists, the upper and lower bounds of a should satisfy

$$\mu_0 f_N (2\epsilon - 1) < \mu_0 f_N (1 - \epsilon) \;\Rightarrow\; \epsilon < 2/3.$$

Note that the decrease of the net sliding error from one iteration to the next is never better than $\frac{a_\epsilon}{a + a_o - a_\epsilon} = \frac{\mu_0 f_N \epsilon}{a + \mu_0 f_N (1 - \epsilon)}$. This gives the lower bound on the feasible convergence rate ρ.

The range of the actual sliding distance can be written as $d_{\text{actual}} \in [d_{\text{goal}} - d_2,\, d_{\text{goal}} + d_3]$, and the error in sliding distance as $e = d_{\text{goal}} - d_{\text{actual}} \in [d_2, -d_3]$.

At each iteration, the error e_k from the previous iteration becomes new $(d_{\text{goal}})_k$ and is used to replan a sliding motion:

$$(d_{\text{goal}})_{k+1} = (d_{\text{goal}})_k - (d_{\text{actual}})_k \in [(d_2)_k\,,\, (-d_3)_k]. \tag{24}$$

To have the error in the net sliding distance converge to zero at least as fast as ρ^k, we need to choose a maximum finger acceleration a_f such that $e_k \le \rho (d_{\text{goal}})_k$. For the case of an overestimated friction coefficient, (3) and (22) show that when $a_f \ge \frac{\mu_0 f_N [\mu_0 f_N (\epsilon - 1)\rho - a(\epsilon + \rho)]}{\mu_0 f_N (\epsilon\rho - \rho + \epsilon) - a\rho}$ we have

$$\frac{|(d_2)_k|}{|(d_{\text{goal}})_k|} \le \frac{a_o + a - a_\epsilon}{a_o + a + a_\epsilon}\rho < \rho. \tag{25}$$

Similarly for the case of an underestimated friction coefficient, (3) and (23) show that when $a_f \ge \frac{\mu_0 f_N [\mu_0 f_N (\epsilon - 1)\rho - a(\epsilon + \rho)]}{\mu_0 f_N (\epsilon\rho - \rho + \epsilon) - a\rho}$ we have

$$\frac{|(d_3)_k|}{|(d_{\text{goal}})_k|} \le \rho. \tag{26}$$

From (22) and (23), we have $d_2 < d_3$ for any $a_f > a_o$. Therefore, we only need to satisfy the a_f constraint that leads to (25), which yields $a_f \ge \frac{\mu_0 f_N [\mu_0 f_N (\epsilon - 1)\rho - a(\epsilon + \rho)]}{\mu_0 f_N (\epsilon\rho - \rho + \epsilon) - a\rho}$.

Combining (24)–(26) gives $\left|\frac{(d_{\text{goal}})_{k+1}}{(d_{\text{goal}})_k}\right| < \rho$, which demonstrates that $|(d_{\text{goal}})_k|$ converges exponentially to zero as the number of iterations k increases. ■

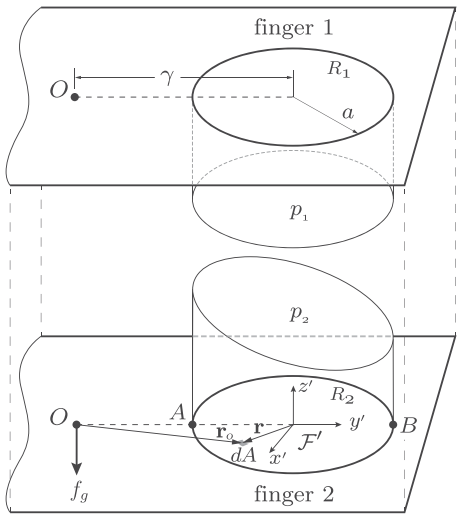

Fig. 20. Contact pressure distribution of the two-fingered pinch grasp.

APPENDIX B
DETAILS OF LIMIT SURFACE MODELING

We introduce a local finger frame $\mathcal{F}_i'$ at the center of the finger, and since the frames $\mathcal{F}_1'$ and $\mathcal{F}_2'$ are coincident in this system, we use $\mathcal{F}'$ to represent the frame as shown in Figs. 10 and 20. The y'-axis is along the direction from the center of the object to the center of the finger. The distance from the CM of the object to the center of the fingers is $\gamma = \left|\, [x_{rf}, y_{rf}]^T \,\right|$.

The contact pressures p_1 and p_2 over the patches are a function of the position on the patch. We have constraints on the pressure distributions to keep the object planar when subject to the spring force, but the exact shape of the pressure distributions is unknown. We chose to approximate the pressure distributions as either constant or linearly varying distributions, as these are the lowest order models that can satisfy the force–moment balance constraints that ensure the planar motion of the object. We assume that modeling errors leading to execution error can be accommodated by our iterative replanning approach.

In particular, the pressure distribution p_1 is assumed to be constant over the contact patch, while p_2 must vary over the contact patch to achieve balance of forces and moments that would otherwise move the object out of the plane. We assume p_2 varies linearly in the y'-direction, as shown in Figs. 10 and 20. The shape of the contact patches are assumed constant and independent of the contact pressures.

A. Mechanics of the System

1) Finger Pressure Distributions: Since the contact pressure of finger 1 is evenly distributed, the total normal force of finger 1 f_{N1} is a function of the spring force S,

$$f_{N1} = \int_{R_1} p_1(\mathbf{r})\, dA = \frac{L_S}{L} S \tag{27}$$

where R_1 is the circular contact region and dA is the infinitesimally small area located at $\mathbf{r} = [x_r, y_r]^T$ with respect to the

local frame $\mathcal{F}'$ as shown in Fig. 20. From (27), we have

$$p_1(\mathbf{r}) = \begin{cases} \frac{L_S S}{\pi a^2 L} & \text{for } |\mathbf{r}| \le a \\ 0 & \text{for } |\mathbf{r}| > a. \end{cases} \tag{28}$$

For finger 2, the contact pressure is assumed to be symmetrical about the y'-axis. Since we assume the shape of the pressure distribution function changes linearly in the y'-direction, as expressed by

$$p_2(\mathbf{r}) = \begin{cases} C_2 + k y_r & \text{for } |\mathbf{r}| \le a \\ 0 & \text{for } |\mathbf{r}| > a \end{cases} \tag{29}$$

where k is the change in pressure dp/dy_r, and C_2 is the constant term of p_2. The total normal force of finger 2 is

$$f_{N2} = \int_{R_2} p_2(\mathbf{r})\, dA = \int_{-a}^{a} \int_{-\sqrt{a^2-y_r^2}}^{\sqrt{a^2-y_r^2}} (C_2 + k y_r) dx_r dy_r$$
$$= \pi a^2 C_2. \tag{30}$$

Since the motion of the system is in the xy plane of $\mathcal{W}$, the total force in the vertical direction and moments about the object CM must be balanced. We denote the total contact moments about the CM of the object as m_{ti}. Therefore, we have

$$m_{t1} = \int_{R_1} [\mathbf{r}_o \times \hat{\mathbf{z}}'] p_1(\mathbf{r})\, dA = \frac{L_S S \gamma}{L} \tag{31}$$

where $\mathbf{r}_o$ is the vector pointing from the object center O to the infinitesimally small area dA, $r_o = [x_r, y_r + \gamma]^T$ as shown in Fig. 20, and $\hat{\mathbf{z}}'$ is the unit vector in $+z'$-direction. For finger 2, we have

$$m_{t2} = \int_{R_2} [\mathbf{r}_o \times \hat{\mathbf{z}}'] p_2(\mathbf{r})\, dA = \frac{\pi a^2}{4}(a^2 k + 4 C_2 \gamma). \tag{32}$$

The force and moment balance equations of the object are

$$f_{N1} + f_{N2} + f_g = 0 \tag{33}$$

$$m_{t1} + m_{t2} = 0. \tag{34}$$

Substituting (27), (30), (31), and (32) into (33) and (34) gives

$$C_2 = -\frac{1}{\pi a^2}\left(f_g + \frac{L_S S}{L}\right) \tag{35}$$

$$k = \frac{4 f_g \gamma}{\pi a^4}. \tag{36}$$

Substituting (35) into (30) gives

$$f_{N2} = -\left(f_g + \frac{L_S S}{L}\right). \tag{37}$$

The finger contacts can only apply forces into the object, which means that for finger 2 the contact pressure at any contact point must be nonnegative, i.e., $\forall \mathbf{r} \in R_2 : p_2(\mathbf{r}) \ge 0$. From (36), we have $k \le 0$. Since $\gamma \ge 0$ and $f_g \le 0$, the minimum contact pressure of finger 2 is the pressure at point B. To ensure feasible contact pressures, $p_2(\mathbf{r}_B) \ge 0$ should be satisfied, where $\mathbf{r}_B = [0, a]^T$. By substituting (29), (35), and (36) into the inequality $p_2(\mathbf{r}_B) \ge 0$, we can solve the maximum distance between the finger center and the object center as

$$\gamma \le \frac{a}{4}\left(1 + \frac{L_S S}{f_g L}\right). \tag{38}$$

When γ exceeds the limit, the contacts break and the object falls out of the grasp since the contacts cannot supply pulling forces. To maintain contacts in this situation, the spring force S should be increased.

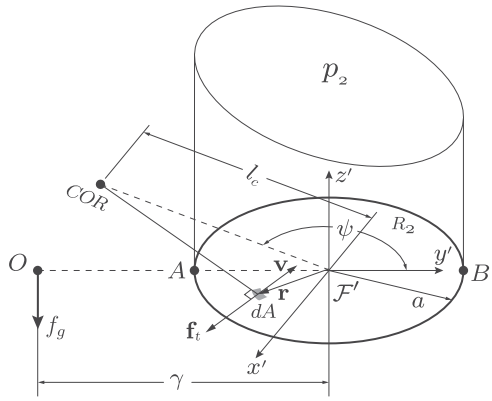

Fig. 21. Close up view of finger 2 pressure distribution.

B. Modeling of Limit Surfaces

1) Constructing Limit Surface Numerically: With the expressions for the finger contact pressure distributions given above, we calculate the frictional forces and moments caused by the contacts for different sliding directions. The set of possible relative velocities at a contact can be parameterized using the center of rotation (COR) formulation as in [25]. The finger's instantaneous COR is defined by two variables: the distance to the center of the finger l_c and the angle from the y'-axis ψ, as shown in Fig. 21. The relative sliding velocity vector at the infinitesimal area dA is $\mathbf{v}$. The tangential frictional force $\mathbf{f}_t$ acts in the opposite direction of $\mathbf{v}$. The total tangential frictional force of each contact is calculated by integrating shear forces over the entire contact patch R_i as

$$\mathbf{f}_{t,i} = \begin{bmatrix} f_{x,i} \\ f_{y,i} \end{bmatrix} = -\int_{R_i} \mu \hat{\mathbf{v}} p_i(\mathbf{r}) dA \tag{39}$$

and the total frictional moment about the z'-axis is

$$m_{z,i} = -\int_{R_i} \mu [\mathbf{r} \times \hat{\mathbf{v}}] p_i(\mathbf{r}) dA \tag{40}$$

where $\hat{\mathbf{v}}$ is the unit vector in the direction of $\mathbf{v}$:

$$\hat{\mathbf{v}} = \frac{1}{\Lambda}\begin{bmatrix} l_c \cos\psi - y_r \\ l_c \sin\psi + x_r \end{bmatrix} \tag{41}$$

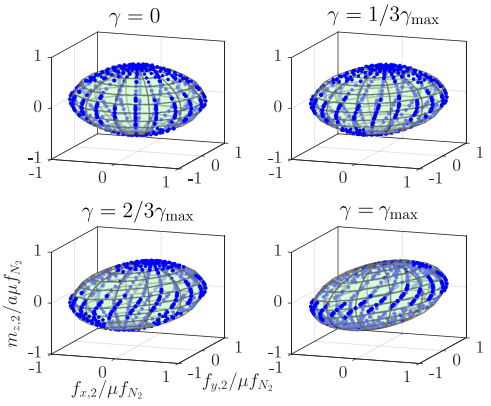

Fig. 22. Numerically integrated and approximated limit surfaces of finger 2. The axes of the friction force space are aligned with the local frame $\mathcal{F}'$ and normalized. Blue dots are the numerical integration results, green ellipsoids show the approximated limit surfaces.

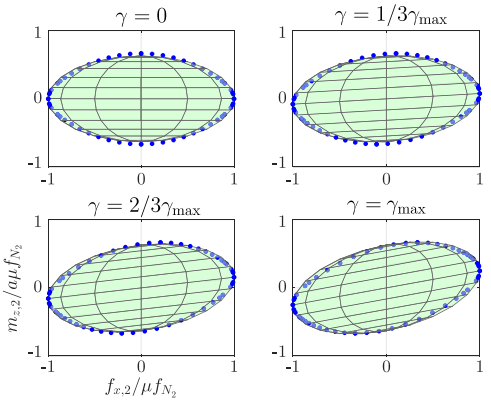

Fig. 23. Numerically integrated and approximated limit surfaces when the COR is moving along the y'-axis, shown in the $f_x m_z$-plane. Blue dots are numerical integration results, green ellipsoids show the approximated limit surfaces.

where $\Lambda = \sqrt{l_c^2 - 2y_r l_c \cos\psi + 2x l_c \sin\psi + x_r^2 + y_r^2}$. Substituting (41) into (39) and (40), we have

$$\mathbf{f}_{t,i} = \int_{-a}^{a} \int_{-\sqrt{a^2-y_r^2}}^{\sqrt{a^2-y_r^2}} \frac{-\mu p_i(\mathbf{r})}{\Lambda} \begin{bmatrix} l_c \cos\psi - y_r \\ l_c \sin\psi + x_r \end{bmatrix} dx_r\, dy_r \tag{42}$$

$$m_{z,i} = \int_{-a}^{a} \int_{-\sqrt{a^2-y_r^2}}^{\sqrt{a^2-y_r^2}} \frac{-\mu\Phi p_i(\mathbf{r})}{\Lambda} dx_r\, dy_r \tag{43}$$

where $\Phi = l_c x_r \sin\psi - l_c y_r \cos\psi + x_r^2 + y_r^2$.

The frictional forces and moments of finger 1 can be considered as a special case of finger 2, where $\gamma = 0$ and both p_1 and p_2 are constant. Therefore, we only analyze the limit surface for finger 2.

Equations (42) and (43) do not have closed-form solutions since they are elliptic integrals. Equations (35) and (36) can be numerically integrated to construct the limit surfaces. Figs. 22 and 23 show the results of numerical integration of limit surfaces of finger 2 with four different values of γ. Each blue dot represents an integration result of a COR position on the $x'y'$-plane (a pair value of l_c and ψ). Substituting $L_S = 0.05$ m, $L = 0.17$ m, $f_g = -0.5$ N, $S = -7$ N, $a = 0.0254$ m into (38), we find the maximum γ is $\gamma_{\max} \approx 1.279$ a.

2) Approximation of the Limit Surfaces: Since the shape of LS_1 is a special case of LS_2 when $\gamma = 0$, in this section we focus on the derivation of the expression for the approximated LS_2. The idea is to fit an ellipsoid to the numerical integrals in the local frame $\mathcal{F}'$ that deforms as γ increases. This LS approximation is then expressed in the local frame $\mathcal{F}^+$, which is used in the dynamics derived in Section V.

Observation 1: From Figs. 22 and 23, we observe that as the distance γ from the object center to the finger center increases, the m_z components of points on the limit surface increase or decrease by a factor linear in both γ and f_x.

From (37), the total normal force is not affected by γ, which means that the maximum linear frictional force μf_{N_2} will be the same as long as $\gamma \leq \gamma_{\max}$, and the projection of the limit surfaces to the $f_x f_y$-plane will be the same circle centered at the origin with radius μf_{N_2}. Equation (36) shows that the contact pressure distribution is determined by γ, which also affects the maximum frictional moment $m_{z,2}$ at each COR. Therefore as γ changes, the shape of the limit surfaces changes in the m_z-direction.

Based on observation 1, we use deformed ellipsoids to approximate the limit surfaces. We denote $\mathbf{f}_e^{\mathcal{F}'} = [f_{x,e}, f_{y,e}, m_{z,e}]^T$ as an arbitrary vector on an ellipsoid centered at the origin of the local finger frame $\mathcal{F}'$, and $\mathbf{f}^{\mathcal{F}'} = [f_x, f_y, m_z]^T$ as an arbitrary vector on the corresponding approximated limit surface. The ellipsoid is represented by

$$(\mathbf{f}_e^{\mathcal{F}'})^T \mathbf{A}_e \mathbf{f}_e^{\mathcal{F}'} = 1 \tag{44}$$

where the matrix $\mathbf{A}_e \in \mathbb{R}^{3\times 3}$ is a symmetric positive-definite matrix that determines the shape of the ellipsoid. In the general ellipsoid definition, $\mathbf{A}_e = \mathrm{diag}(s_1^{-2}, s_2^{-2}, s_3^{-2})$ where s_1, s_2, and s_3 represent the lengths of the semiprincipal axes. We again assume isotropic dry friction so the maximum tangential force the contact can resist is $s_1 = s_2 = \mu|f_{N_i}|$. The maximum moment along the normal direction is $s_3 = ca\mu|f_{N_i}|$, where a is the radius of the contact patch and c is a constant from numerical integration. Here, we take $c = 0.63$ based on the findings in [25].

Since the limit surface is approximated by the ellipsoid deformed linearly in the m_z-direction proportional to f_x, we have

$$m_z = m_{z,e} + \kappa(\gamma) f_{x,e} \tag{45}$$

where $\kappa(\gamma)$ is a variable that determines the linear mapping.

To derive $\kappa(\gamma)$, we choose a critical point $\mathbf{f}_*^{\mathcal{F}'} = [f_x^*, f_y^*, m_z^*]^T$ in the frame $\mathcal{F}'$. Let $f_x^* = \mu f_{N_2}$, $f_y^* = 0$ so the projection of $\mathbf{f}_*^{\mathcal{F}'}$ in the $f_x f_y$-plane is at the edge of the limit circle. At this point, from the ellipsoid definition, we have $m_{z,e}^* = 0$. From (45), we find

$$\kappa(\gamma) = m_z^* / f_{x,e}^*. \tag{46}$$

We calculate m_z^* from (36) and (43) by substituting $\psi = 0$ and $l_c = -\infty$

$$m_z^* = -\mu \int_{-a}^{a} \int_{-\sqrt{a^2-y_r^2}}^{\sqrt{a^2-y_r^2}} y_r(C_2 + k y_r) dx_r dy_r$$
$$= -\frac{\mu \pi a^4 k}{4} = -\mu f_g \gamma. \quad (47)$$

Since the ellipsoid is only deformed in the m_z-direction, we have $f_{x,e}^* = f_x^* = \mu f_{N_2}$. Substituting this expression and (47) into (46), we have

$$\kappa(\gamma) = \frac{m_z^*}{f_x^*} = -\frac{f_g \gamma}{f_{N_2}}. \quad (48)$$

The transformation from the ellipsoid to the limit surface is given by

$$\left(\mathbf{f}^{\mathcal{F}'}\right)^T = \left(\mathbf{f}_e^{\mathcal{F}'}\right)^T \mathbf{D} \quad (49)$$

where $\mathbf{D}$ is an affine transformation matrix that deforms the ellipsoid as

$$\mathbf{D} = \begin{bmatrix} 1 & 0 & \kappa \\ 0 & 1 & 0 \\ 0 & 0 & 1 \end{bmatrix}.$$

From (44) and (49), we have $(\mathbf{f}^{\mathcal{F}'})^T \mathbf{D}^{-1} \mathbf{A}_e \mathbf{D}^{-T} \mathbf{f}^{\mathcal{F}'} = 1$. The expression for all the points on the limit surface can be written as

$$\left(\mathbf{f}^{\mathcal{F}'}\right)^T \mathbf{A}_m \mathbf{f}^{\mathcal{F}'} = 1 \quad (50)$$

where

$$\mathbf{A}_m = \mathbf{D}^{-1} \mathbf{A}_e \mathbf{D}^{-T} = \begin{bmatrix} (\kappa^2/s_3^2 + s_1^{-2}) & 0 & -\kappa/s_3^2 \\ 0 & s_2^{-2} & 0 \\ -\kappa/s_3^2 & 0 & s_3^{-2} \end{bmatrix}.$$

To describe the frictional limit surface in the frame $\mathcal{F}^+$, we have

$$\mathbf{f}^T = \left(\mathbf{f}^{\mathcal{F}'}\right)^T \mathbf{R}^{\mathcal{F}'\mathcal{F}^+} \quad (51)$$

where $\mathbf{R}^{\mathcal{F}'\mathcal{F}^+}$ is a transformation matrix that transfers the reference frame of linear force vectors from $\mathcal{F}'$ to $\mathcal{F}^+$ and

$$\mathbf{R}^{\mathcal{F}'\mathcal{F}^+} = \begin{bmatrix} \sin\phi & -\cos\phi & 0 \\ \cos\phi & \sin\phi & 0 \\ 0 & 0 & 1 \end{bmatrix}$$

where $\phi = \tan^{-1}(\frac{y_{rf2}}{x_{rf2}})$, as shown in Fig. 6. From (50) and (51), we write the equation of the limit surface in frame $\mathcal{F}^+$ as

$$\mathbf{f}^T \mathbf{A} \mathbf{f} = 1 \quad (52)$$

where $\mathbf{A} = (\mathbf{R}^{\mathcal{F}'\mathcal{F}^+})^{-1} \mathbf{A}_m (\mathbf{R}^{\mathcal{F}'\mathcal{F}^+})^{-T}$.

Comparisons showing the good agreement between the approximated frictional limit surface and the numerically integrated points are shown in Figs. 22 and 23.

REFERENCES

[1] D. E. Whitney, "Quasi-static assembly of compliantly supported rigid parts," *J. Dyn. Syst., Meas. Control*, vol. 104, no. 1, pp. 65–77, 1982.

[2] S. Huang and J. M. Schimmels, "Admittance selection for force-guided assembly of polygonal parts despite friction," *IEEE Trans. Robot.*, vol. 20, no. 5, pp. 817–829, Oct. 2004.

[3] N. Chavan-Dafle *et al.*, "Extrinsic dexterity: In-hand manipulation with external forces," in *Proc. IEEE Int. Conf. Robot. Autom.*, May 2014, pp. 1578–1585.

[4] J. Shi, J. Woodruff, and K. Lynch, "Dynamic in-hand sliding manipulation," in *Proc. 2015 IEEE/RSJ Int. Conf. Intell. Robots Syst.*, Sep. 2015, pp. 870–877.

[5] Z. Li, P. Hsu, and S. Sastry, "Grasping and coordinated manipulation by a multifingered robot hand," *The Int. J. Robot. Res.*, vol. 8, no. 4, pp. 33–50, 1989.

[6] T. Yoshikawa and K. Nagai, "Manipulating and grasping forces in manipulation by multifingered robot hands," *IEEE Trans. Robot. Autom.*, vol. 7, no. 1, pp. 67–77, Feb. 1991.

[7] N. Rojas and A. Dollar, "Characterization of the precision manipulation capabilities of robot hands via the continuous group of displacements," in *Proc. IEEE/RSJ Int. Conf. Intell. Robots Syst. Conf.*, Sep. 2014, pp. 1601–1608.

[8] D. Brock, "Enhancing the dexterity of a robot hand using controlled slip," in *Proc. IEEE Conf. Robot. Autom.*, Apr. 1988, vol. 1, pp. 249–251.

[9] A. Cole, P. Hsu, and S. Sastry, "Dynamic control of sliding by robot hands for regrasping," *IEEE Trans. Robot. Autom.*, vol. 8, no. 1, pp. 42–52, Feb. 1992.

[10] J. Trinkle and J. Hunter, "A framework for planning dexterous manipulation," in *Proc. IEEE Int. Conf. Robot. Autom.*, Apr. 1991, vol. 2, pp. 1245–1251.

[11] M. Yashima, Y. Shiina, and H. Yamaguchi, "Randomized manipulation planning for a multi-fingered hand by switching contact modes," in *Proc. IEEE Int. Conf. Robot. Autom.*, vol. 2, Sep. 2003, pp. 2689–2694.

[12] R. Fearing, "Simplified grasping and manipulation with dextrous robot hands," *IEEE J. Robot. Autom.*, vol. 2, no. 4, pp. 188–195, Dec. 1986.

[13] M. Cherif and K. K. Gupta, "Global planning for dexterous reorientation of rigid objects: Finger tracking with rolling and sliding," *The Int. J. Robot. Res.*, vol. 20, no. 1, pp. 57–84, 2001.

[14] N. Furukawa, A. Namiki, S. Taku, and M. Ishikawa, "Dynamic regrasping using a high-speed multifingered hand and a high-speed vision system," in *Proc. IEEE Int. Conf. Robot*, May 2006, pp. 181–187.

[15] N. Chavan-Dafle and A. Rodriguez, "Prehensile pushing: In-hand manipulation with push-primitives," in *Proc. 2015 IEEE/RSJ Int. Conf. Intell. Robots Syst.*, Sep. 2015, pp. 6215–6222.

[16] F. E. Viña, B. Y. Karayiannidis, K. Pauwels, C. Smith, and D. Kragic, "In-hand manipulation using gravity and controlled slip," in *Proc. 2015 IEEE/RSJ Int. Conf. Intell. Robots Syst.*, Sep. 2015, pp. 5636–5641.

[17] F. E. Viña, B. Y. Karayiannidis, C. Smith, and D. Kragic, "Adaptive control for pivoting with visual and tactile feedback," in *Proc. 2016 IEEE Int. Conf. Robot. Autom.*, May 2016, pp. 399–406.

[18] V. Kumar, E. Todorov, and S. Levine, "Optimal control with learned local models: Application to dexterous manipulation," in *Proc. 2016 IEEE Int. Conf. Robot. Autom.*, May 2016, pp. 378–383.

[19] A. Sintov and A. Shapiro, "Swing-up regrasping algorithm using energy control," in *Proc. 2016 IEEE Int. Conf. Robot. Autom.*, May 2016, pp. 4888–4893.

[20] Y. Hou, Z. Jia, A. M. Johnson, and M. T. Mason, "Robust planar dynamic pivoting by regulating inertial and gripping forces," in *Workshop Algorithmic Found. Robot.*, 2016.

[21] H. Arisumi, K. Yokoi, and K. Komoriya, "Casting manipulation—Midair control of a gripper by impulsive force," *IEEE Trans. Robot.*, vol. 24, no. 2, pp. 402–415, Apr. 2008.

[22] S. Goyal, "Planar sliding of a rigid body with dry friction: Limit surfaces and dynamics of motion," Ph.D. dissertation, Cornell Univ., Ithaca, NY, USA, 1989.

[23] S. Goyal, A. Ruina, and J. Papadopoulos, "Planar sliding with dry friction—Part 1. Limit surface and moment function," *Wear*, vol. 143, no. 2, pp. 307–330, 1991.

[24] S. Goyal, A. Ruina, and J. Papadopoulos, "Planar sliding with dry friction —Part 2. Dynamics of motion," *Wear*, vol. 143, no. 2, pp. 331–352, 1991.

[25] N. Xydas and I. Kao, "Modeling of contact mechanics and friction limit surfaces for soft fingers in robotics, with experimental results," *The Int. J. Robot. Res.*, vol. 18, no. 9, pp. 941–950, 1999.

[26] J. Zhou, R. Paolini, J. A. Bagnell, and M. T. Mason, "A convex polynomial force-motion model for planar sliding: Identification and application," in *Proc. IEEE Int. Conf. Robot. Autom.*, May 2016, pp. 372–377.

Jian Shi received the B.S. degree in mechanical engineering and automation from Beihang University, Beijing, China, in 2011. He is currently working toward the Ph.D. degree in mechanical engineering at Northwestern University, Evanston, IL, USA.

His research interests include motion planning and control of dynamic robot manipulation.

J. Zachary Woodruff (S'15) received the B.S. degree in mechanical engineering from University of Notre Dame, Notre Dame, IN, USA, in 2013, and the M.S. degree in mechanical engineering from Northwestern University, Evanston, IL, USA, in 2016. He is a mechanical engineering Ph.D. candidate at Northwestern University in the Neuroscience and Robotics Lab (nxr.northwestern.edu).

His research interests include motion planning and control for hybrid dynamical systems with uncertainty.

Mr. Woodruff received the National Science Foundation Graduate Research Fellowship in 2015.

Paul B. Umbanhowar received the B.A. degree in physics from Carleton College, Northfield, MN, USA, in 1987, and the Ph.D. degree in physics from The University of Texas at Austin, Austin, TX, USA, in 1996.

He is a Research Associate Professor in the Department of Mechanical Engineering, Northwestern University, Evanston, IL, USA, and an affiliate member of the Neuroscience and Robotics Laboratory. His research interests include locomotion on yielding substrates, frictional and vibratory manipulation, and flow, segregation, and mixing of granular materials.

Kevin M. Lynch (S'90–M'96–SM'05–F'10) received the B.S.E. degree in electrical engineering from Princeton University, Princeton, NJ, USA, in 1989, and the Ph.D. degree in robotics from Carnegie Mellon University, Pittsburgh, PA, USA, in 1996.

He is a Professor and the Chair of the Mechanical Engineering Department, Northwestern University, Evanston, IL, USA. He is a member of the Neuroscience and Robotics Laboratory and the Northwestern Institute on Complex Systems. His research interests include dynamics, motion planning, and control for robot manipulation and locomotion; self-organizing multiagent systems; and functional electrical stimulation for restoration of human function. He is a coauthor of the textbooks *Principles of Robot Motion* (MIT Press, 2005), *Embedded Computing and Mechatronics* (Elsevier, 2015), and *Modern Robotics: Mechanics, Planning, and Control* (Cambridge University Press, 2017).